ADVANCED FUNCTIONAL MATERIALS

Supporting Information

for *Adv. Funct. Mater.*, DOI: 10.1002/adfm.201700336

Cu Diffusion-Driven Dynamic Modulation of the Electrical Properties of Amorphous Oxide Semiconductors

*Han-Wool Yeon, Janghyun Jo, Hochul Song, Youngho Kang, Sekwon Na, Hyobin Yoo, Seung-Yong Lee, Haelim Cho, Ho-Young Kang, Jung-Kyu Jung, Seungwu Han, Miyoung Kim, and Young-Chang Joo**

Supporting Information

Cu Diffusion-Driven Dynamic Modulation of the Electrical Properties of Amorphous Oxide Semiconductors

*Han-Wool Yeon, Janghyun Jo, Hochul Song, Youngho Kang, Sekwon Na, Hyobin Yoo, Seung-Yong Lee, Haelim Cho, Ho-Young Kang, Jung-Kyu Jung, Seungwu Han, Miyoung Kim, and Young-Chang Joo**

Electrical analysis of the devices

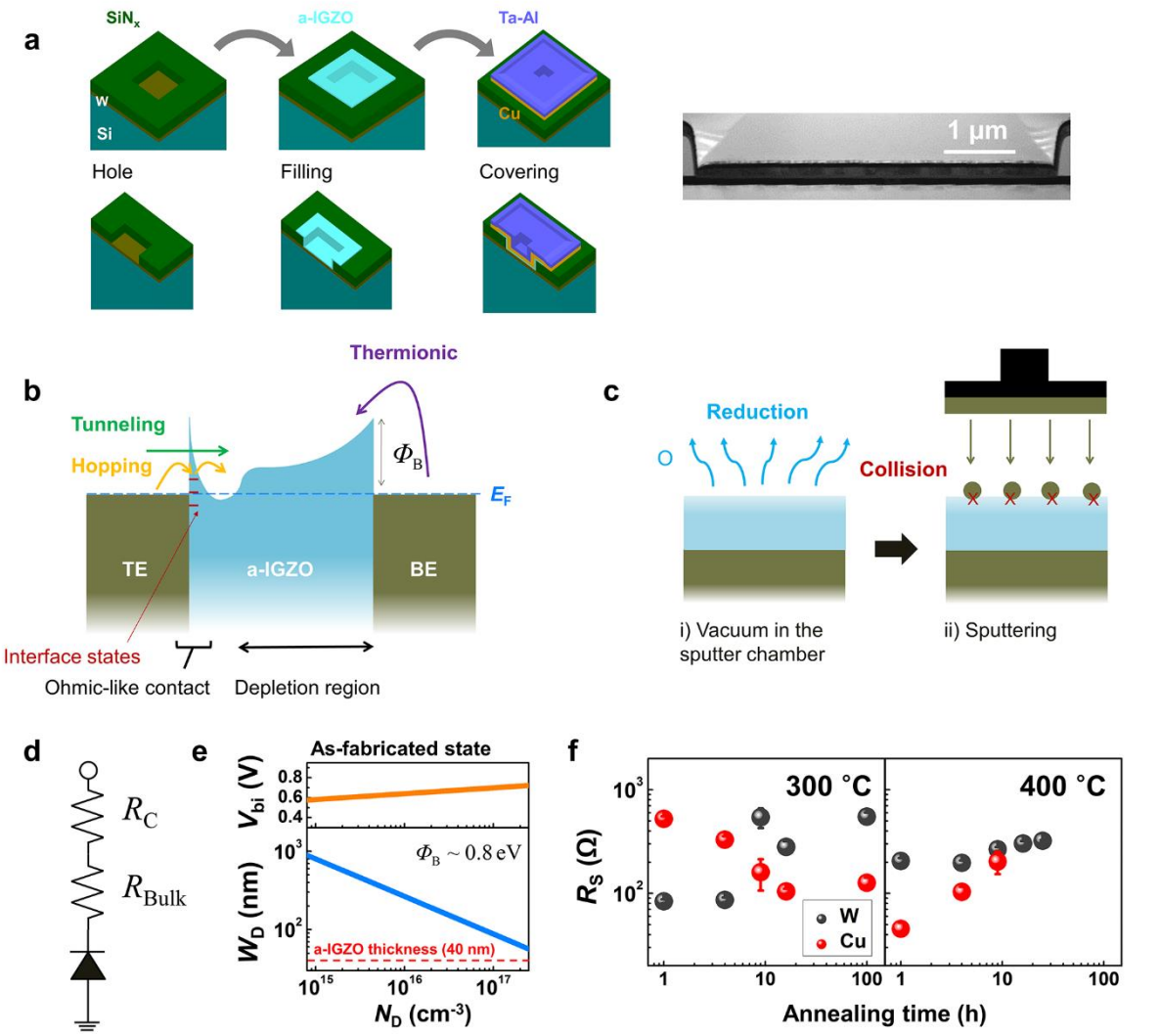

Figure S1. Schematics of (a) fabrication processes for the devices, (b) energy band diagram, (c) possible mechanisms of the interface state generation at the TE/a-IGZO interfaces during the TE deposition process, and (d) equivalent circuits of the devices. A cross-sectional TEM image of the 25 μm^2 Cu devices in the as-fabricated state is also shown in the right of Figure S1a. (e) V_{bi} and W_D in the a-IGZO in the as-fabricated devices. (f) Changes in the R_S values in the 25 μm^2 devices as a function of the annealing temperature and time.

Figure S1a depicts the fabrication processes for the devices. A cross-sectional transmission electron microscope (TEM) image of the 25 μm^2 Cu devices in the as-fabricated state is shown in the right of Figure S1a. An asymmetric current-voltage (*I-V*) characteristics indicate that the electrical conduction of the devices is strongly affected by the Schottky barrier at the metal/amorphous In-Ga-Zn-O (a-IGZO) interface. As noted in the main article, the Schottky

barrier height (Φ_B) at the a-IGZO/bottom electrode (BE) interface is higher than at the a-IGZO/TE interface because the electrical conductance (G) of the devices is higher under a negative bias than under a positive bias. Furthermore, the current under a negative bias exhibits exponential behavior as a function of the applied voltage, whereas a weak voltage-dependent current is shown under a positive bias. These results strongly suggest that the dominant conduction mechanism of the Schottky conducting devices is thermionic emission governed by a Schottky barrier at a-IGZO/BE interfaces.[1] When forward bias (i.e., negative bias) with $V = 3k_BT/q$ (~80 mV at 25 °C) is applied, the subsequent *I-V* characteristics would be as follows:[1],[2]

$$I_{FORWARD} = I_S \exp\left(\frac{qV - I_{FORWARD}R_S}{nk_BT}\right) \quad (1)$$

where q is the electron charge, k_B is the Boltzmann's constant, T is the absolute temperature, I_S is the saturation current, n is the ideality factor, and R_S is the series resistance of the devices. I_S is expressed as[1],[2]

$$I_S = AA^*T^2 \exp\left(-\frac{\Phi_B}{k_BT}\right), \quad (2)$$

where A is the contact area (4-2500 μm^2) and A^* is the effective Richardson constant (theoretically A^* =40.8 A cm^{-2} K^{-2} for a-IGZO[3]). We measured Φ_B and n in the voltage range of 0.1-0.2 V (i.e., the linear region in the semi-logarithmic *I-V* curve) at room temperature (RT), and R_S was estimated from the slope of the $I/(dI/dV)$ - I curve.[4]

Figure S1b depicts the energy band diagram of the TE/a-IGZO/W-BE structures. The ideal Φ_B at W/a-IGZO interfaces was calculated based on the ideal electron affinity of a-IGZO (χ_{IGZO}) and the ideal work function (Φ_F) of W, $\Phi_B = \Phi_F - \chi_{IGZO}$.[1] An ideal χ_{IGZO} can be estimated considering the molar percentage of In, Ga, and Zn and the electron affinity of the corresponding metal oxides, In_2O_3, Ga_2O_3, and ZnO.[3] For the a-IGZO thin-film patches in

the devices, as the molar percentage of In, Ga, and Zn were 0.55, 0.55, and 0.9, respectively, the value of χ_{IGZO} was estimated to be 3.99 eV. Because Φ_F of the W is 4.55 eV,[5] the ideal Φ_B at W/a-IGZO interfaces is calculated to be 0.56 eV. In the as-fabricated state, Φ_B of the devices was estimated to be ~0.8 eV higher than the ideal value of approximately 0.2 eV. This result is the opposite of previous reports, in whicih Φ_B at metal/a-IGZO Schottky interfaces tends to have a smaller value than the ideal Φ_B due to Fermi level (E_F) pinning at the localized state in the band gap of a-IGZO.[6],[7]

In this study, a W-BE surface might be unintentionally oxidized (WO_x) and/or nitrated (WN_y) during annealing at 300 °C in ambient air before the deposition of the SiN_x isolation layer and/or during the SiNx isolation layer. If W-BE is oxidized or nitrated, Φ_B exhibits a higher value than the ideal Φ_B because oxidation and/or nitration increases the Φ_F value of W (6.7 eV and ~5 eV for WO_3 and WN_y, respectively).[8],[9] However, no significant oxidation or nitration have occurred because XPS analysis did not detect WO_x and WN_y at the a-IGZO/W-BE interface, and the results only showed metallic W^0, as shown in Figure S28. A transmission electron microscopy (TEM) analysis did not observe any interfacial layer between a-IGZO and W-BE (Figure S8-S23). Nevertheless, we speculate that although no oxidation and/or nitration of W-BE was detected by XPS and TEM, very small amounts of WO_x and/or WN_y might exist at the W-BE surface and induce the higher Φ_F of W compared to pure W, resulting in a higher Φ_B value than the ideal Φ_B.

Figure S1c illustrates the possible mechanisms of defect generation at the TE/a-IGZO interfaces during the TE deposition process. First, the a-IGZO surface would be reduced in the vacuum chamber before TE material sputtering.[2] Thus, increases in the doping concentration (i.e., V_0 concentration) decrease the barrier width and assist barrier tunneling conduction.[10] Second, sputtering processes can generate defects on the a-IGZO surface as the

energetic TE materials change in terms of the chemical states of In, Ga, Zn, or O[11] (i.e., changes in the bonding network of a-IGZO or the generation of undercoordinated ions[12]). These various and complex defects may increase the doping concentration or act as hopping sites, resulting in a decrease in the effective Φ_B as depicted in Figure S1b.[10] Similar to our results showing that Φ_B at the top interface is lower than that at the bottom interfaces. Lee et al. reported that when a Schottky contact is formed at the bottom interface of an a-IGZO thin film, the Φ_B is higher than that of an a-IGZO Schottky diode composed of a Schottky barrier at the top interface.[11] Moreover, Chasin et al. reported that when metals are deposited onto a-IGZO, the Schottky barrier at the TE interfaces is negligible (quasi-ohmic contact), regardless of the value of the work function of the metals.[12] These results support our deductions.

Figure S1d presents the equivalent circuits of the Schottky conducting devices, of which R_S is the summation of contact resistance at the TE/a-IGZO interfaces (R_C) and the bulk resistance of the undepleted region in the a-IGZO thin-film patches (R_{BULK}). To estimate the contribution of R_{BULK} on R_S, the width of depletion region in the a-IGZO thin-film patches (W_D) in the as-fabricated devices was calculated using the following equation:[1]

$$W_D = \sqrt{\frac{2\varepsilon_{IGZO}\varepsilon_0 V_{bi}}{qN_D}}, \quad (3)$$

where ε_{IGZO} is the relative dielectric constant (10 for a-IGZO[3]), ε_0 is the permittivity of vacuum, N_D is the doping concentration of a-IGZO, and V_{bi} is the built-in potential. An assumption of this equation is that N_D is uniform, and a donor donates a single electron ($N_D \rightarrow N_D^+ + e^-$). Although V_O can donate two electrons at most ($V_O \rightarrow V_O^{n+} + ne^-$, , n=1,2),[13] we assumed that V_O solely exhibits 1+ charge. V_{bi} is expressed as[1]

$$V_{bi} = \frac{1}{q}\left[\Phi_B - (E_C - E_F)_{a\text{-}IGZO}\right] = \frac{1}{q}\left[\Phi_B + k_B T \ln\left(\frac{N_D}{N_C}\right)\right], \quad (4)$$

where E_C is the conduction band minmum of a-IGZO, and N_C is the effective density of conduction band states (5×10^{18} cm^{-3} for a-IGZO[3]). As the Φ_B of the devices is ~0.8 eV and N_D is below 10^{16} cm^{-3} in the as-fabricated state (below the detection limit of Hall measurement[14]), V_{bi} and W_D at RT were calculated as shown in Figure S1e. An ideal W_D is thicker than a-IGZO (40 nm). Thus, in ideal conditions, N_D is uniform, a-IGZO is fully depleted, and R_S in the as-fabricated state is strongly affected by R_C rather than R_{BULK}. However, in the actual devices, N_D is not uniform because of the interfacial states at the TE interfaces. Non-uniform N_D may induce an undepleted region in a-IGZO in the as-fabricated devices. Details of the influence of the interface defects at TE interfaces on W_D are discussed in Figure S2.

Figure S1f shows the R_S of the Schottky conducting W devices and Cu devices with respect to the annealing conditions (contact area of 25 μm^2). After annealing at 300 °C for 1 h, the R_S of both devices decreased compared to that of the as-fabricated state (Figure 1b). However, the R_S of the Cu devices was still higher than that of the W devices. After an annealing time of 9 h, the R_S of the annealed W devices at 300 °C increased. We previously reported an increase in the R_S of the W devices after annealing.[14] The increase in R_S is strongly correlated with the decrease in G of the W devices (Figure 1d in the main text). The increase in R_S indicates that the R_C of the W devices increased during an annealing time of 9 h, as R_{BULK} (i.e., the electrical conductivity of a-IGZO) tends to decrease after annealing due to structural relaxation (SR)-driven doping.[14] Furthermore, the increase in R_C implies that the defect density at the W-TE/a-IGZO interfaces decreased during annealing. The plausible mechanism of the reduction in the interface state density is the recovery of broken bonds (i.e., atomic rearrangement) in the W-TE/a-IGZO interfaces during annealing.[15] An important

point is that the values of R_S, Φ_B and n remained nearly constant after annealing times of 9 h to 100 h, whereas those of the Cu devices continuously changed as the annealing time elapsed. The dependence on the annealing time of the electrical properties of the Cu devices indicates that Cu diffusion-driven doping significantly affected the electrical properties of the Cu devices. On the other hand, the weak dependence on the annealing time of the electrical properties of the W devices indicates that SR is a dominant origin of the changes in the electrical properties of the W devices: the degree of SR (i.e., densification of the amorphous network) is determined by the annealing temperature rather than the annealing time.[16-18]

Under annealing at 400 °C, minimum values of the R_S of the Cu devices were observed for 1 h, and the R_S of the Cu devices gradually increased as the annealing time increased, whereas that of the W devices remained nearly constant. These phenomena support that concentration of Cu-related defects continuously increased with annealing time, whereas the concentration of donor-state Cu is saturated within annealing time of 1 h, resulting in observation of decrease of electrical conductivity of a-IGZO after annealing for 16 h (Figures 1c and 1d).

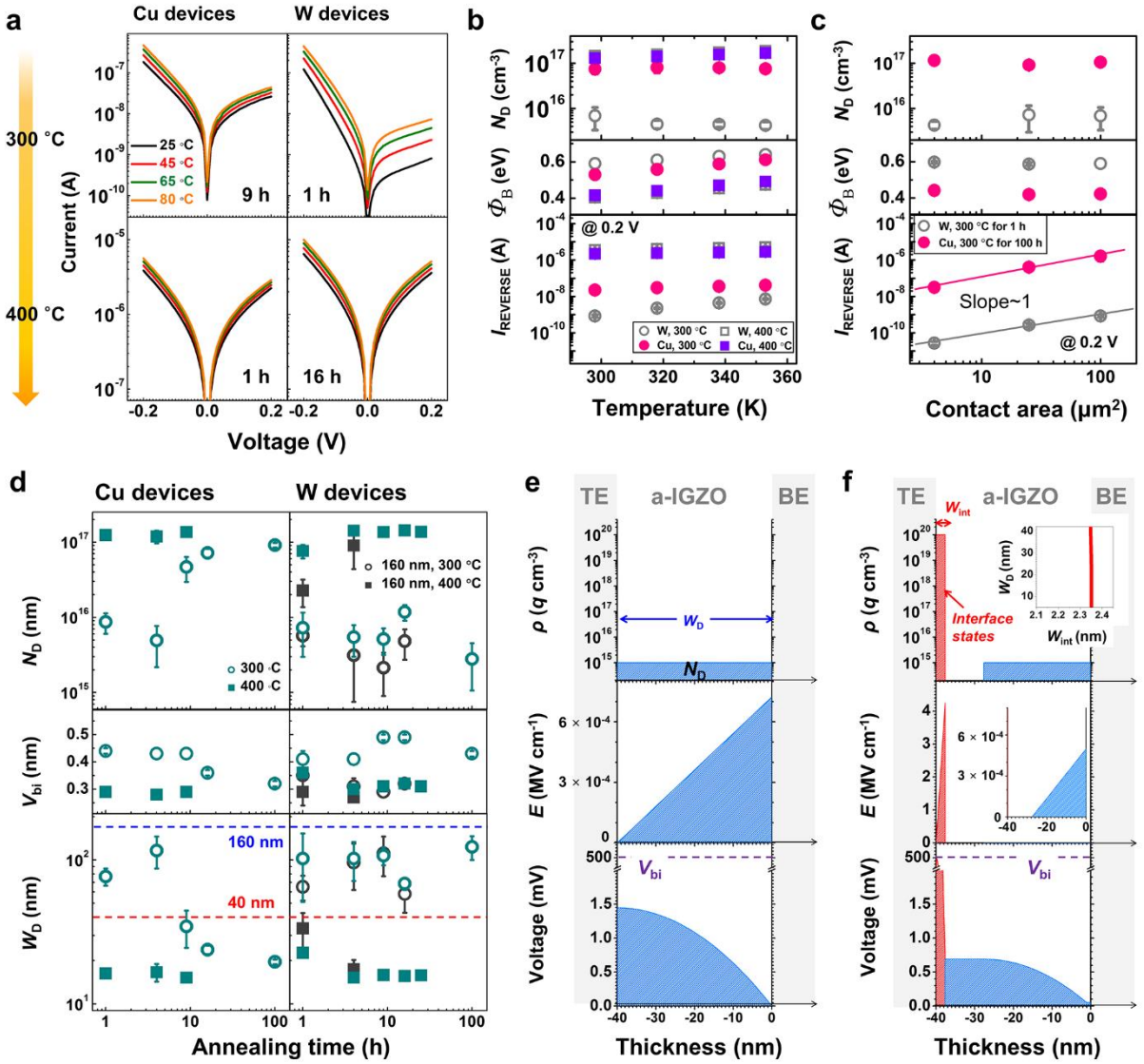

Figure S2. (a) Representative *I-V* cures of the devices after annealing at 300-400 °C with respect to the substrate temperature. Dependence of $I_{REVERSE}$, Φ_B, and N_D on the (b) substrate temperature and (c) contact area of the devices after annealing. (d) The changes of N_D in the Schottky conducting devices estimated by reverse current analysis. V_{bi} and W_D were also calculated from the N_D values. Distributions of space charge density (ρ), electric field (E), and electrostatic potential in a-IGZO (e) without or (f) with interfacial states at the TE interfaces.

The decrease in Φ_B with increasing n of the Schottky conducting devices qualitatively implies that N_D in a-IGZO increases (top of Figure 1e).[2] Furthermore, for the quantitative analysis of N_D in the Schottky conducting devices, we have analyzed the reverse leakage current ($I_{REVERSE}$). Analyzing the capacitance (C) characteristics of semiconductors in the Schottky diodes has been an effective method to estimate the doping concentration in

semiconductors.[1],[4] However, the Schottky conducting devices in this study have parasitic capacitors, induced by the isolation layer and the large size of TE covering the a-IGZO patches, which prohibited the estimation of C of a-IGZO thin-film patches in the devices. The details of the peculiar C characteristics of the Schottky conducting devices are shown in our previous report.[14] For these reasons, we have estimated the N_D in the Schottky conducting devices by analyzing the electrical conduction behavior under reverse bias. As the reverse bias (V_R) increases Φ_B decreases, resulting in increase in $I_{REVERSE}$.[1],[6] When V_R is higher than $3k_BT/q$ (80-90 mV at 25-80 °C), $I_{REVERSE}$ is then[1],[6]

$$I_{REVERSE} = I_S \exp\left(\frac{\Delta\Phi_B}{k_BT}\right), \quad (5)$$

where $\Delta\Phi_B$ is the magnitude of Schottky barrier lowering, which is expressed by,

$$\Delta\Phi_B = 2^{-3/4}\pi^{-1/2}q^{7/4}(\varepsilon_{IGZO}\varepsilon_0)^{-3/4}N_D^{1/4}(V_R + V_{bi} - k_BT/q)^{1/4}. \quad (6)$$

Substituting equation (4) into equation (6) gives

$$\Delta\Phi_B = 2^{-3/4}\pi^{-1/2}q^{7/4}(\varepsilon_{IGZO}\varepsilon_0)^{-3/4}N_D^{1/4}\left[V_R + \frac{1}{q}\left(\Phi_B + k_BT\,ln\left(\frac{N_D}{N_C}\right) - k_BT\right)\right]^{1/4}. \quad (7)$$

If the devices are stable under high V_R, in excess of V_{bi}, then N_D can be extracted based on the slope of semi-logarithmic $I_{REVERSE} - V_R^{1/4}$ plot. However, electrical breakdown occurred in the devices under a V_R of < 6 V (Figure 3 in the main text and Figure S4e). For this reason, the value of N_D was extracted by analytical calculation using equations (2), (5), and (7) and the experimental values of Φ_B and $I_{REVERSE}$ at V_R (> $3k_BT/q$). Furthermore, the substrate temperature and contact area dependence of N_D were measured to estimate the accuracy of the extracted value of N_D.

Figure S2a presents a typical *I-V* curve of the W and Cu devices (contact area of 100 μm^2) after annealing at 300 °C and 400 °C with respect to the substrate temperature and the

corresponding Φ_B, $I_{REVERSE}$ at 0.2 V (> $3k_BT/q$), and the calculated N_D values are shown in Figure S2b. The number of devices under tests (DUTs) was at least 5. Although $I_{REVERSE}$ increases with substrate temperature, the value of N_D remains relatively constant. Figure S2c also shows that the extracted N_D value is not affected by the contact area of the devices. These results suggest that the N_D values obtained by analyzing the reverse current characteristics (top of Figure 1e and top of Figure S2d) are fairly reliable.

A notable fact is that when W_D in the a-IGZO is calculated using N_D, V_{bi}, and equation (3), W_D is greater than the physical thickness of a-IGZO (40 nm) in the devices when N_D is 10^{15}~10^{16} cm^{-3}, as shown at the bottom of Figure S2d. Accordingly, when a-IGZO, whose N_D is 10^{15}~10^{16} cm^{-3}, is fully depleted, V_{bi} should exhibit a value far below the extracted V_{bi} (middle of Figure S2d). Figure S2e shows that when the space charge density (ρ) is solely composed of N_D of 10^{15} cm^{-3}, 1.45 mV of V_{bi} is formed under full depletion of a-IGZO.

A notable fact is that when W_D in the a-IGZO is calculated using N_D, V_{bi}, and equation (3), W_D is greater than the physical thickness of a-IGZO (40 nm) in the devices when N_D is 10^{15}~10^{16} cm^{-3}, as shown at the bottom of Figure S2d. Accordingly, when a-IGZO, whose N_D is 10^{15}~10^{16} cm^{-3}, is fully depleted, V_{bi} should exhibit a value far below the extracted V_{bi} (middle of Figure S2d). Figure S2e shows that when the space charge density (ρ) is solely composed of N_D of 10^{15} cm^{-3}, 1.45 mV of V_{bi} is formed under full depletion of a-IGZO. In Figure S2e, the distributions of the electric field (E) and electrostatic potential (V) according to a-IGZO thickness (x) were calculated based on the equations $dE/dx = \rho/(\varepsilon_{IGZO}\varepsilon_0)$ and $dE/dx = -V$, respectively.[15] These results may imply that the extracted N_D of 10^{15} ~ 10^{16} cm^{-3} has the potential to be an inaccurate value.

However, in the actual devices, ρ in the vicinity of the TE interface would be much higher than in the a-IGZO bulk because interface defects such as V_O s are generated during the TE deposition process (Figure S1c), which is strongly supported by the negligible Φ_B at the TE/a-IGZO interface compared to Φ_B at a-IGZO/BE interfaces. Thus, the high concentration of defect density at the TE interfaces, whose values are expected to be ~10^{20} cm^{-3} for quasi-ohmic contact,[2] would be the dominant origin of V_{bi} in the devices. This phenomenon (i.e., non-uniform distribution of ρ) has been referred to as hetero-size charging in nano-sized systems.[19] Figure S2e depicts the effect of the interfacial charge density at the TE interfaces on the distribution of the electric field and electrostatic potential of the devices. In the analytical calculation, V_{bi} and N_D of bulk a-IGZO are set as 500 mV and 10^{15} cm^{-3}, respectively. When the interface charge at the TE interfaces (10^{20} cm^{-3}) is distributed in 2.3 nm of thickness, the W_D of a-IGZO is calculated to be 29.6 nm, and undepleted regions exist in a-IGZO thin-films [An inset in Figure S2e presents the changes in W_D with respect to the width of interfacial space charges at the TE interface (W_{int}).] In this case, the extracted N_D value of 10^{15} cm^{-3} would make sense.

Above all, our previous results showed that although the a-IGZO thickness in the W devices increased to 160 nm, which is greater than W_D, the tendency of N_D changes with respect to post-fabrication annealing were very similar to changes in W devices composed of 40-nm-thick a-IGZO (Our previous results are included in Figure S2d.).[14] Therefore, we believe that the N_D obtained by reverse current analysis is also quite accurate for devices composed of 40-nm-thick a-IGZO thin films.

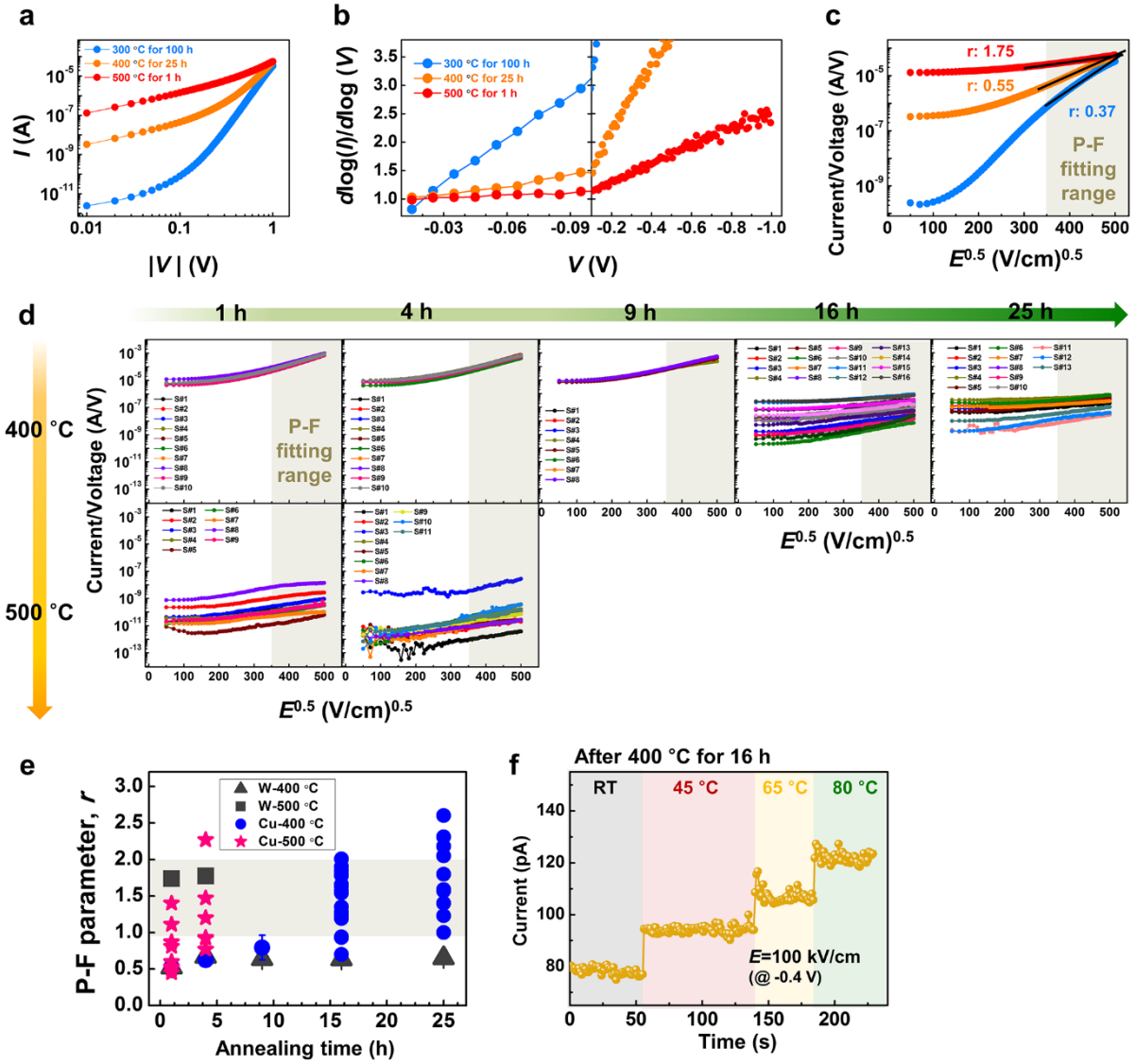

Figure S3. (a) Double-logarithmic *I-V* plot of W devices after annealing at 300-500 °C under negative bias condition. (b) The slope of the corresponding plots to determine the ohmic conduction. (c) Log(I/V)-$E^{0.5}$ plots of the *I-V* curves in Figure S3a. (d) Log(I/V)-$E^{0.5}$ plots of the 25 μm^2-Cu devices after annealing at 400-500 °C to identify the P-F conduction. (e) P-F fitting results of the Cu devices and the W devices (contact area of 25 μm^2). (f) Substrate temperature dependence of the electrical current of the 25 μm^2-Cu devices after annealing at 400 °C for 16 h at E=100 kV/cm.

Figure S3a presents typical *I-V* curves of the W devices (contact area of 4 μm^2) after anneal ing at 300-500 °C under negative bias conditions. As the annealing temperature increases to 5 00 °C, the slope of the double-logarithmic *I-V* curves decreases to 1 in the low-voltage region (< 0.1 V), as shown in Figure S3b. Thus, in the low-voltage region, the conduction mechanis m of the W devices exhibiting symmetric *I-V* curves is ohmic conduction, whereas Schottky c

onducting devices did not. As the applied voltage increased, the conduction mechanism of the W devices after annealing at 500 °C transformed to non-ohmic conduction.

Figure S3c presents the $\log(I/V)$ vs. $\sqrt{E}$ plot for the *I-V* curves in Figure S3a, which was used to determine that the dominant conduction mechanism is P-F conduction (i.e., bulk-limit ed conduction). The P-F conduction is given as[20,21]

$$I_{\text{P-F}} \propto E\exp\left[\frac{1}{rk_{\text{B}}T}\left(q\sqrt{\frac{qE}{\pi\varepsilon_{\text{IGZO}}\varepsilon_0}}-\Phi_{\text{PF}}\right)\right] \quad (8)$$

where E is approximately V divided by 40 nm, Φ_{PF} is the P-F barrier, and r is a constant ranging from 1 to 2.[20,21] The parameter r is derived from the slope of the $\log(I/V)$ vs. $\sqrt{E}$ curve in the range of 350 to 500 $\sqrt{\text{kV/cm}}$. When the W devices produce rectifying *I-V* curve s, the calculation of r for the devices yields a value below 1. These results indicate that the d ominant conduction mechanism of the W devices exhibiting asymmetric *I-V* curves is not P-F conduction, but rather Schottky thermionic emission. However, when the *I-V* curves of the W devices are symmetrical (after annealing at 500 °C), the calculation of r values yields ~1.8, in dicating that P-F conduction is the dominant conduction mechanism (Figure S3e). The conduc tion mechanism consists of ohmic conduction in the low-field region and P-F conduction in th e high-field region, which is analogous to previous reports on the conduction mechanisms of a morphous materials including a-IGZO.[2],[22]

Figure S3d presents the $\log(I/V)$ vs. $\sqrt{E}$ plot for the Cu devices after annealing at 400-5 00 °C under negative bias conditions. Like the W devices, the Cu devices exhibiting asymme tric *I-V* curves have r of below 1, as shown in Figure S3e. These results also indicate that th e dominant conduction mechanism of the Cu devices is Schottky thermionic emission, which the *I-V* characteristics exhibit rectifying behavior. Although some of the Cu devices that exhi bit symmetric *I-V* curves matched well to P-F fitting, the variation in the r values of the Cu devices was wide (Figure S3e), similar to the variation in G (Figure 1d in the main text). Th

us, the dominant conduction mechanism of the Cu devices deviates from orthodox P-F cond uction theory. If tunneling-based conduction, another bulk-limited conduction, were the dom inant conduction mechanism of the Cu devices, G would be weakly dependent on the substr ate temperature.[1] However, G of the Cu devices increased as the substrate temperature incr eased, as shown in Figure S3f. Therefore, P-F conduction or tunneling-based conduction is n ot the dominant conduction mechanism of the Cu devices which exhibit non-polar electrical conduction and complex conduction mechanisms exist.

Table S1. Summary of the characteristics of a-IGZO-based RS devices.

TE	BE	RS type	Proposed atomic origin of RS	Distinction of the study	RS ratio [10^n]	Endurance [10^n]	Retention [10^n s]	Ref.
Ti TiN Pt	TiN Ti	Uni Bi	V_O	Influence of electrode material	2	2	-	23
W Au	Pt Au Al ITO	Uni		Influence of electrode material	-	-	-	24
ITO	ITO	Bi		Demonstration of transparent memory	1	2	4 (90 °C)	25
Pt	TiN	Uni		Influence of O stoichiometry	>1	-	-	26
Cu	Cu	Uni		Demonstration of Flexible memory	2~3	~2	-	27
Al	Al	Bi		Influence of Ga, O stoichiometry	<1	2	-	28
Pt	Pt	Bi		Analog switching (synaptic behavior)	-	-	-	29
Ti TiN	Pt	Bi		Influence of electrode material and O stoichiometry	~1	4	-	30
Pt	Pt	Bi		UV-irradiation on solution-processed a-IGZO	~1	2	4 (25 °C)	31
Ni	ITO	Bi		Integration with *p*-type NiO films	~2	3	5 (25 °C)	32
Ag	Pt	Bi		Influence of Ru doping	~5	~1	-	33
Ag	Pt	Bi	Ag	Influence of O stoichiometry	~2	2	4 (25 °C)	34
Ag	Pt	Bi		Integration with SiO_2 thin films	3	2	4 (85 °C)	35

Table S1 summarizes the characteristics of the a-IGZO-based resistive switching (RS) devices reported to date. Note that most studies have suggested that RS is induced by the anion (or equivalently the oxygen vacancy, V_O) migration, except Supporting refs. 34 and 35, which reported Ag migration-driven RS. Thus, our study is the first report of Cu migration-based RS behavior in a-IGZO thin films.

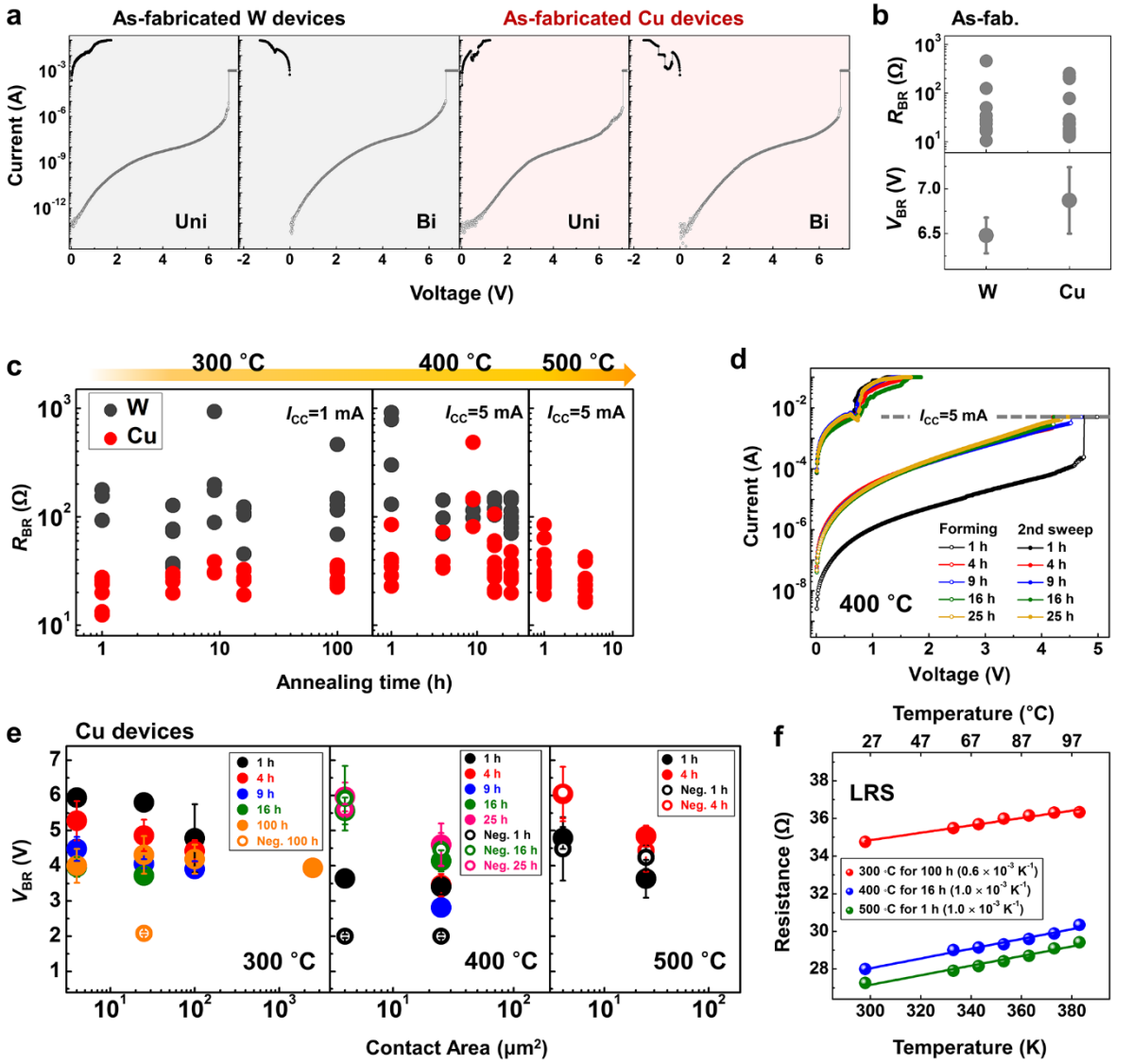

Figure S4. (a) Typical breakdown behavior of the 25-μm^2 as-fabricated devices with respect to the operating bias polarity (unipolar, bipolar). (b) V_{BR} and R_{BR} of the 25-μm^2 as-fabricated devices. (c) R_{BR} of the 25-μm^2 annealed devices. (d) Typical breakdown characteristics of the 25 μm^2-W devices after annealing at 400 °C. (e) Area dependence of the breakdown voltage or V_{FORM} of the Cu devices. (f) Temperature dependence of the resistance of the 25 μm^2-Cu devices at LRS under unipolar RS.

Figure S4a presents the typical breakdown characteristics of the as-fabricated W devices and Cu devices (contact area of 25 μm^2). Both devices exhibited irreversible breakdown (i.e., hard breakdown, HDBR) regardless of the operating bias polarity, unipolar and bipolar bias conditions. In the as-fabricated state, breakdown voltage (V_{BR}) of the W devices is similar to (or slightly lower than) that of the Cu devices as shown in Figure S4b. Furthermore, the W

devices and the Cu devices exhibited similar resistance value after electrical breakdown (R_{BR}). However, as Cu doping occurred, trend of V_{BR} and R_{BR} between the W devices and the Cu devices was changed as shown in Figure 3c in the main text and Figure S4c, respectively. Figure S4c presents the R_{BR} of the W devices and Cu devices with respect to the annealing conditions. The contact area of the devices was 25 μm^2. Most of the W devices showed higher R values than those of the Cu devices, although the compliance current (I_{CC}) conditions were the same and the breakdown voltage of the W devices was higher than that of the Cu devices, as shown in Figure 3c. Thus, although less power was consumed to break the Cu devices compared to the W devices, the conductive paths of the Cu devices were more conducting than those of the W devices. These results indicate that Cu ions significantly affect the formation of conductive paths in the Cu devices, whereas intrinsic defects such as oxygen vacancies (V_Os) are the dominant component of the conductive paths in the W devices. The W devices annealed at 400 °C exhibited HDBR behavior regardless of the annealing time up to 25 h as shown in Figure S4d.

Figure S4e shows the contact-area dependence of the breakdown voltage of the Cu devices with respect to the annealing conditions. Regardless of the contact area, the tendency of the br eakdown voltage changes due to Cu diffusion is the same: the V_{BR} decreases as the annealing temperature increases. However, as the contact area increases, the V_{BR} of the Cu devices show s a decreasing tendency under the same annealing conditions. These phenomena represent the nature of dielectric breakdown. Dielectric breakdown occurs through the vertical linkage of de fects in the dielectric medium that is sufficient to electrically interconnect the top and bottom electrodes, known as percolation paths[36,37] or conductive filaments (CFs).[38] The formation o f CFs is initiated from the lateral defects in dielectrics.[37] Thus, as the contact area increases, t he number of lateral defects (i.e., breakdown spots) increases, resulting in a decrease in break down voltage as well as the degradation of dielectric reliability (i.e., decreased time to breakd

own).[39,40] In addition to the Cu devices annealed at 300 °C for 100 h, the Cu devices anneale d at 400 °C for 16 h and 500 °C for 1 h showed positive temperature coefficient of resistance (TCR) values at LRS, as shown in Figure S4f. The TCR was extracted based on the equation, $R(T) = R_0[1+\alpha(T - T_0)]$, where R_0 is the resistance at temperature T_0, 273 K, and α is the T CR.[41] These results imply that although the dominant role of the Cu is to reduce the electrical conductivity of a-IGZO, enough donor-state mobile Cu still exists in a-IGZO to form metallic CFs, generating unipolar RS.

First-principles calculations

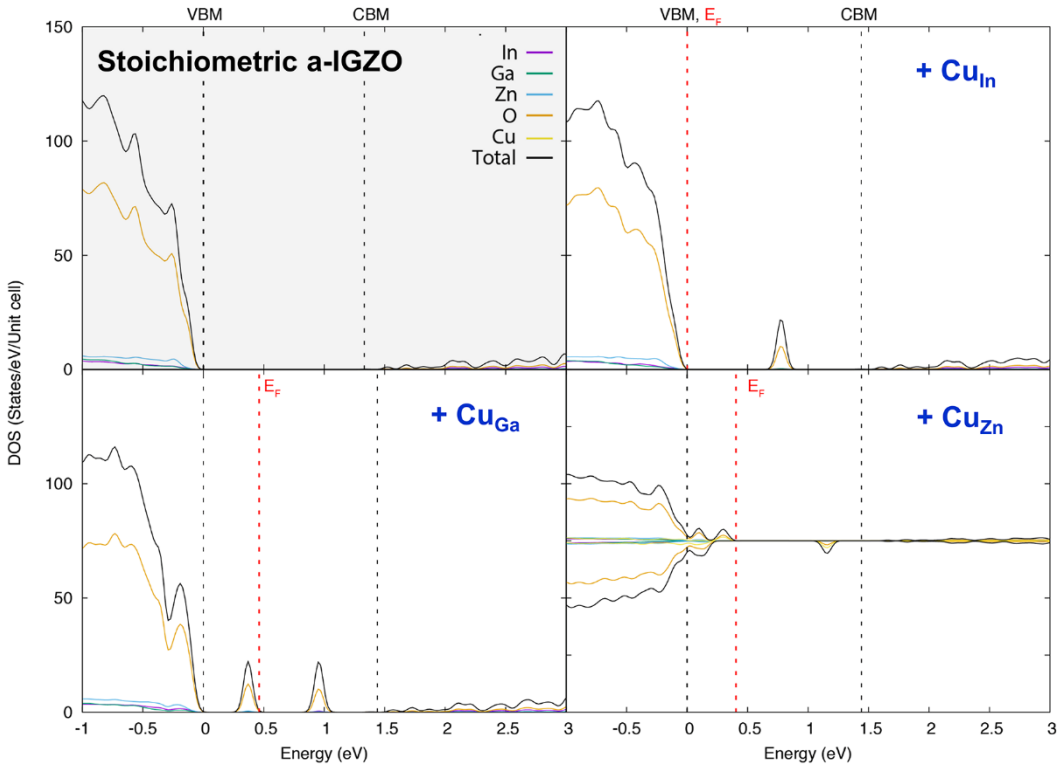

Figure S5. The changes in the total and partial DOS of stoichiometric a-IGZO due to Cu doping at the substitutional sites, In, Ga, or Zn. The substituting Cu sites generated empty levels in the band gap. Cu in the free volume generated filled levels inside the conduction band, which can act as electron donors, whereas the empty levels in the band gap generated by the substituting Cu can act as acceptor-like traps. Note that the actual efficiency of substitutional Cu doping in *ionic* a-IGZO would be poor compared to the corresponding crystalline oxides, as the local charge neutrality of the substitutional dopant is apt to be maintained (i.e., charge compensation) in an *ionic* bonding-based amorphous structure.[41-43]

Statistical analysis of RS performance in the Cu devices

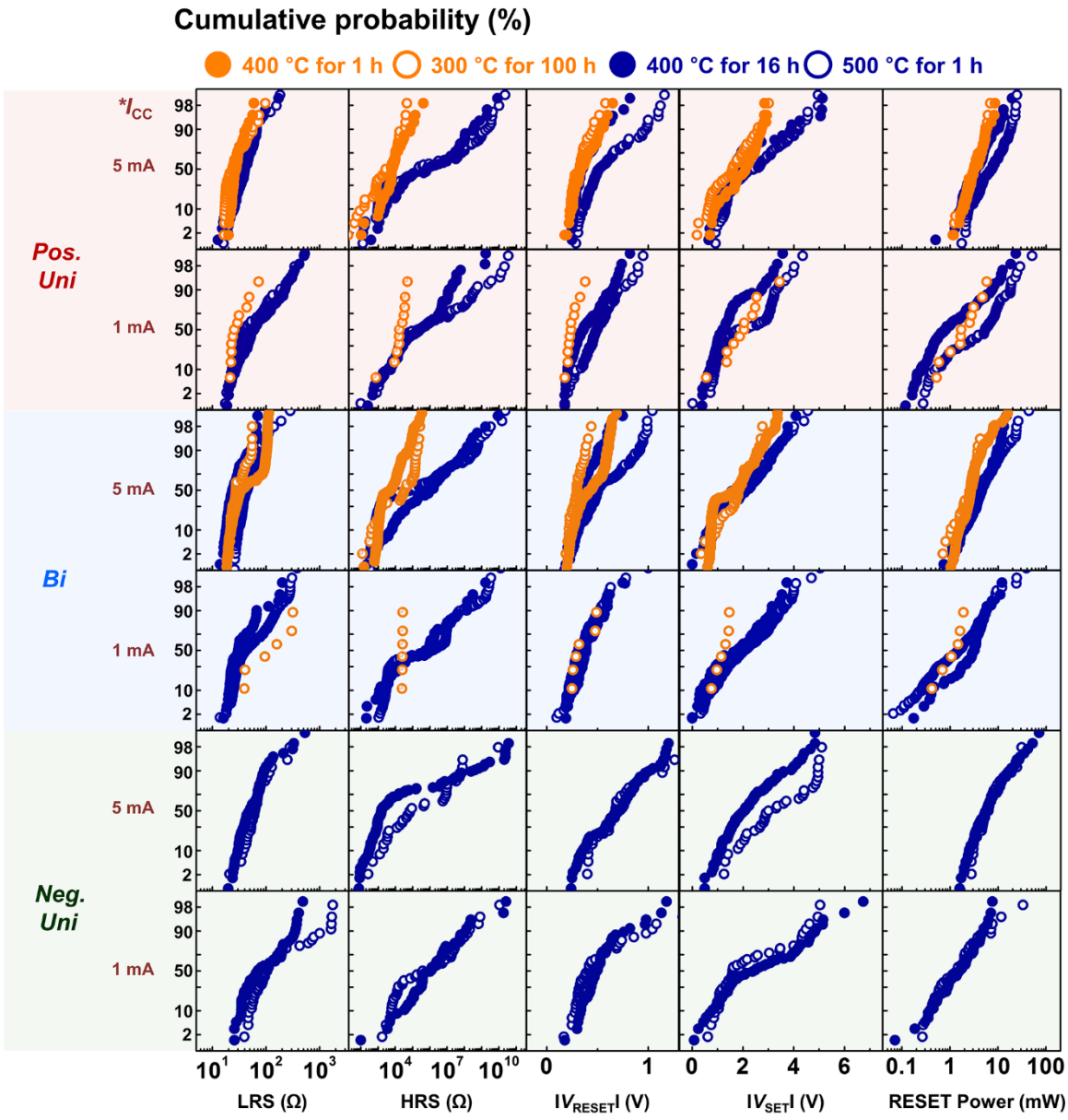

Figure S6. Cumulative distributions of the electrical resistance at the LRS/HRS, SET/RESET voltage, and RESET power in the 4 μm^2-Cu devices (300 °C for 100 h, 400 °C for 1 h or 16 h, and 500 °C for 1 h) with respect to bias polarity conditions as well as the I_{CC} values.

Figure S6 presents the cumulative distributions of the resistive switching (RS) performances (resistance, voltage, and RESET power) of the 4 μm^2-Cu devices following the method described in the JEDEC standard JESD 37: The number of the DUTs was at least 5 per bias polarity conditions, except for the annealed Cu devices at 300 °C for 100 h under an

I_{CC} of 1 mA (1 DUT). As noted in the main text, RS performance is determined by the dominant role of the Cu dopant in a-IGZO, whether a mobile electron donor or Cu-related defects which decrease the electrical conductivity of a-IGZO. When the mobile Cu donor is dominant, the RS performance is superior to the Cu devices, which have significant Cu-related defects that are Cu-In-O clusters shown in Figure 4 in the main text. Therefore, suppression of Cu-In-O clusters is a prerequisite for the improvement of RS performance.

When negative bias is applied for RESET, electrochemical oxidation occurs at the CFs and assists the Joule heating-induced CF rupture.[44,45] Thus, it can be expected that the RESET power consumption is reduced under negative unipolar condition or bipolar bias condition compared to positive unipolar condition.[46,47] Unfortunately, among the Cu devices, this prediction solely turned occurred for the Cu devices annealed at 500 °C for 1 h under an I_{CC} of 1 mA: when I_{CC} increases to 5 mA, the difference in the RESET power consumption under bias polarity conditions disappeared. These results imply that the contribution of electrochemical oxidation to CF rupture is negligible and Joule heating is the dominant driving force of CF rupture.

As I_{CC} decreased from 5 mA to 1 mA, resistance at the LRS increased, whereas resistance at the HRS remained nearly constant, regardless of the bias polarity conditions. Moreover, the RESET power consumption also decreased. These phenomena were more clearly observed under negative unipolar RS conditions than under unipolar RS or bipolar RS conditions. In previous reports, the resistance at the LRS showed a decreasing tendency against increasing I_{CC} because the amount of electrochemically reduced mobile cations increased, resulting in an increase in the thickness (or the number) of the CFs.[48,49] Therefore, these results indicate the promise of Cu-doped a-IGZO in application to multi-level memristive devices.[49] The decrease in the RESET power consumption can be explained by the reduced need for Joule

heating for the rupture of thinner (or fewer) CFs. When the I_{CC} is reduced more than 1 mA, electrochemical oxidation may significantly affect CFs rupture, in addition to Joule heating, resulting in a decrease in the RESET power consumption.[46]

Transmission electron microscopy (TEM)

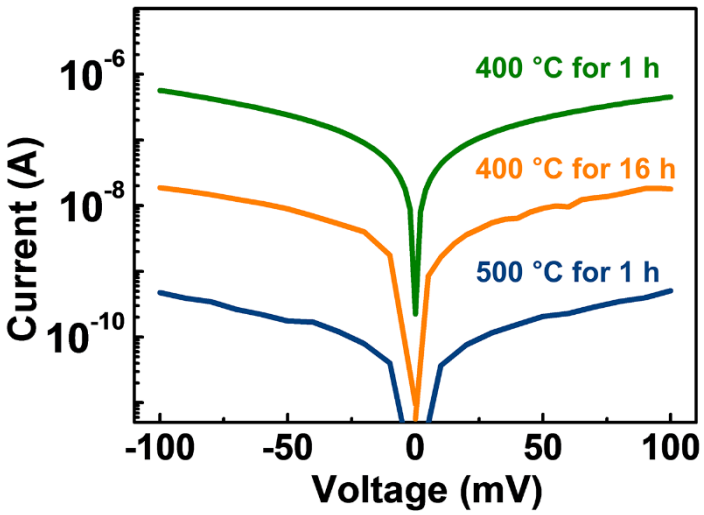

Figure S7. *I-V* characteristics of the annealed Cu devices before preparing the TEM samples: 400 °C for 1 h and 16 h and 500 °C for 1 h. The contact area of the devices was 25 μm^2. The maximum applied voltage was 100 mV, which was small compared to the electrical breakdown voltage of the Cu devices, to minimize the influence of electrical stress on microstructural changes. These results confirm that the Cu devices used for the TEM samples had similar electrical properties to other the Cu devices and hence, these samples represent the microstructural properties of the Cu devices with respect to the annealing conditions.

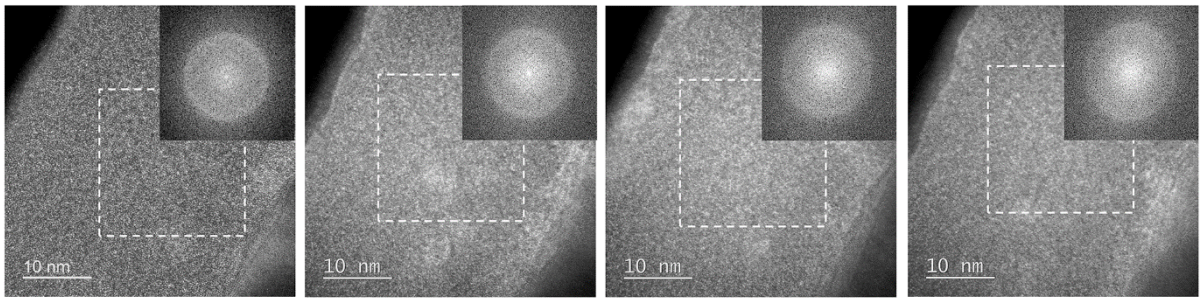

Figure S8. HRTEM images of the Cu devices after annealing at 400 °C for 1 h. The FFT diffractograms from the selected region (white-dotted line) show that the amorphous phase was maintained after annealing at 400 °C for 1 h.

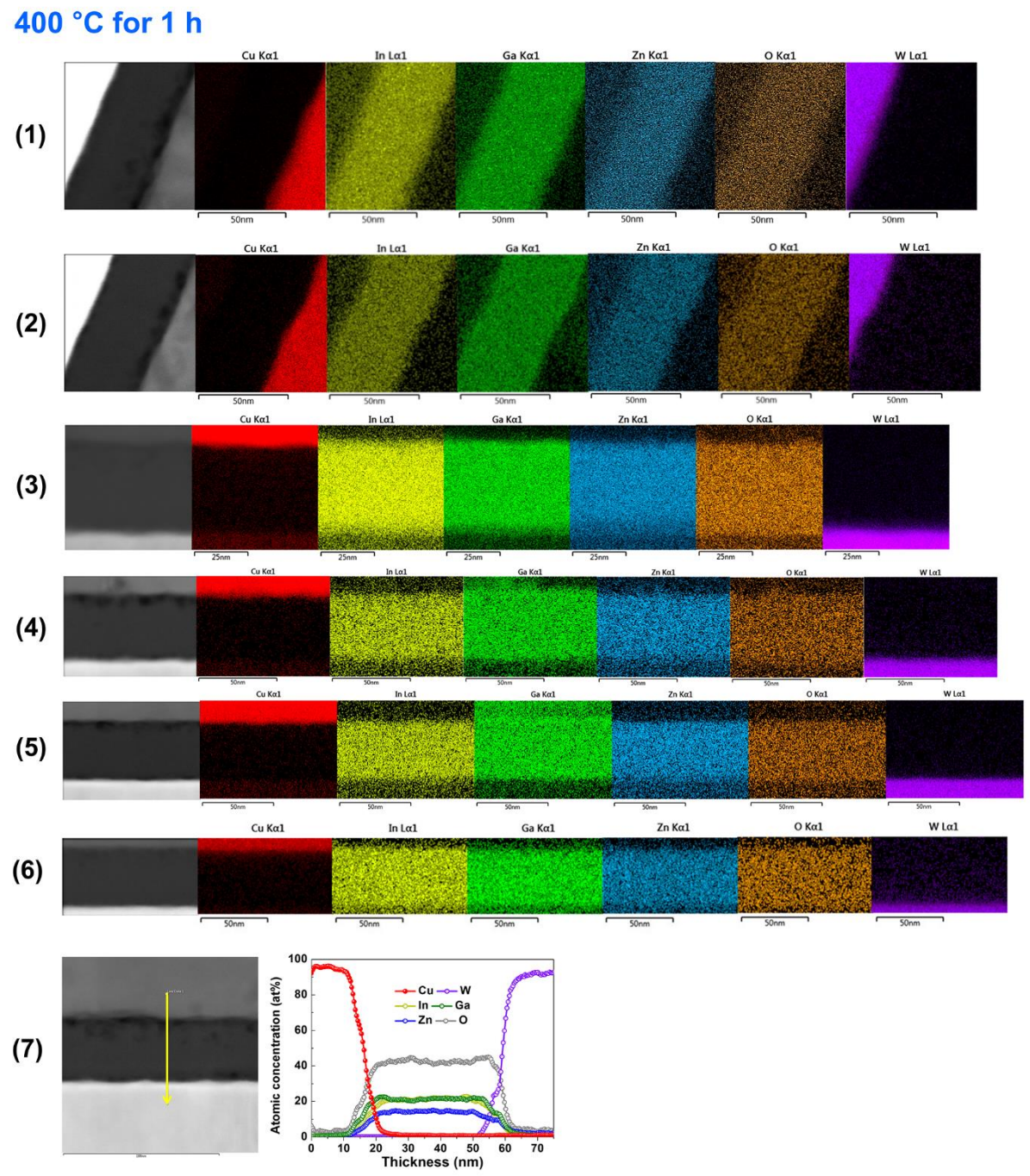

Figure S9. EDS maps and line profiles of the Cu devices after annealing at 400 °C for 1 h. Cu was not detected in the a-IGZO thin-film patches.

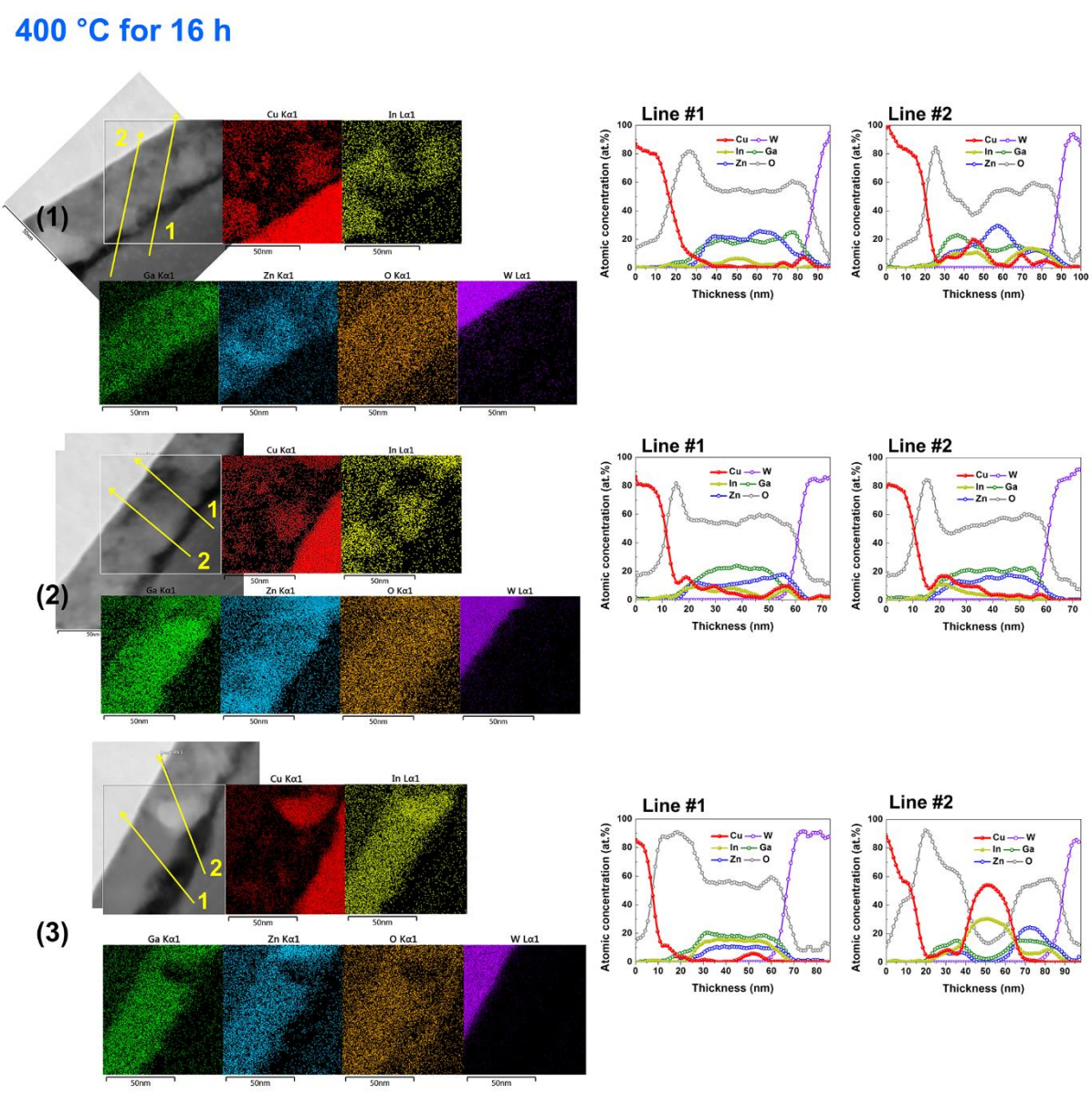

Figure S10. EDS maps and line profiles of the Cu devices after annealing at 400 °C for 16 h, Areas 1-3. The Cu were non-uniformly distributed in a-IGZO. In congregated in Cu-rich clusters, whereas In concentration severely decreased compared to Ga or Zn in the a-IGZO bulk. Thus, *In-doped Cu-rich clusters* formed in a-IGZO after Cu diffusion.

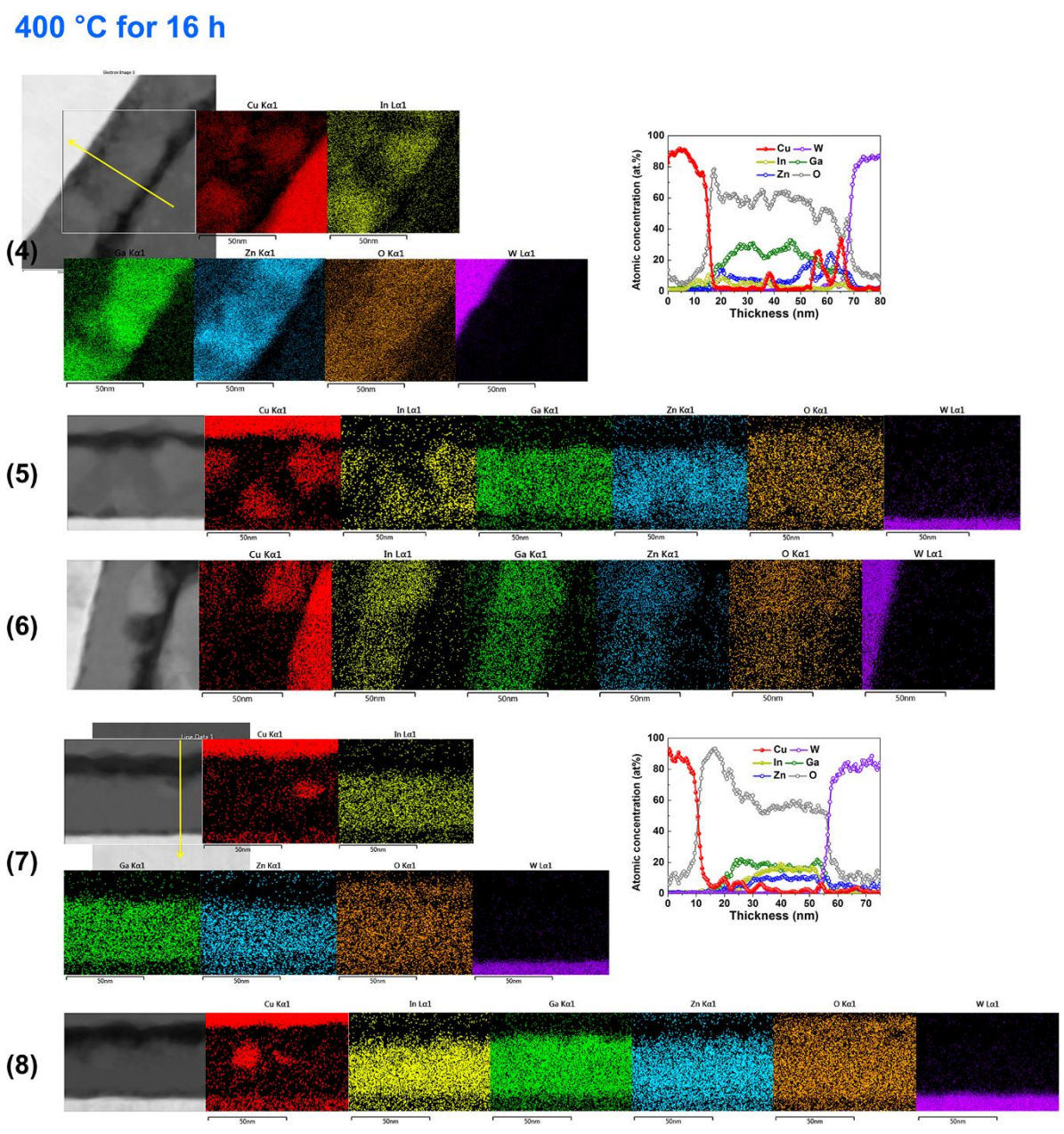

Figure S11. EDS maps and line profiles of the Cu devices after annealing at 400 °C for 16 h, Areas 4-8. In Areas 4-6, In-doped Cu-rich clusters were observed whereas some of the Cu-rich clusters did not contain significant amounts of In as shown in Areas 7 and 8 (*mainly Cu-O*).

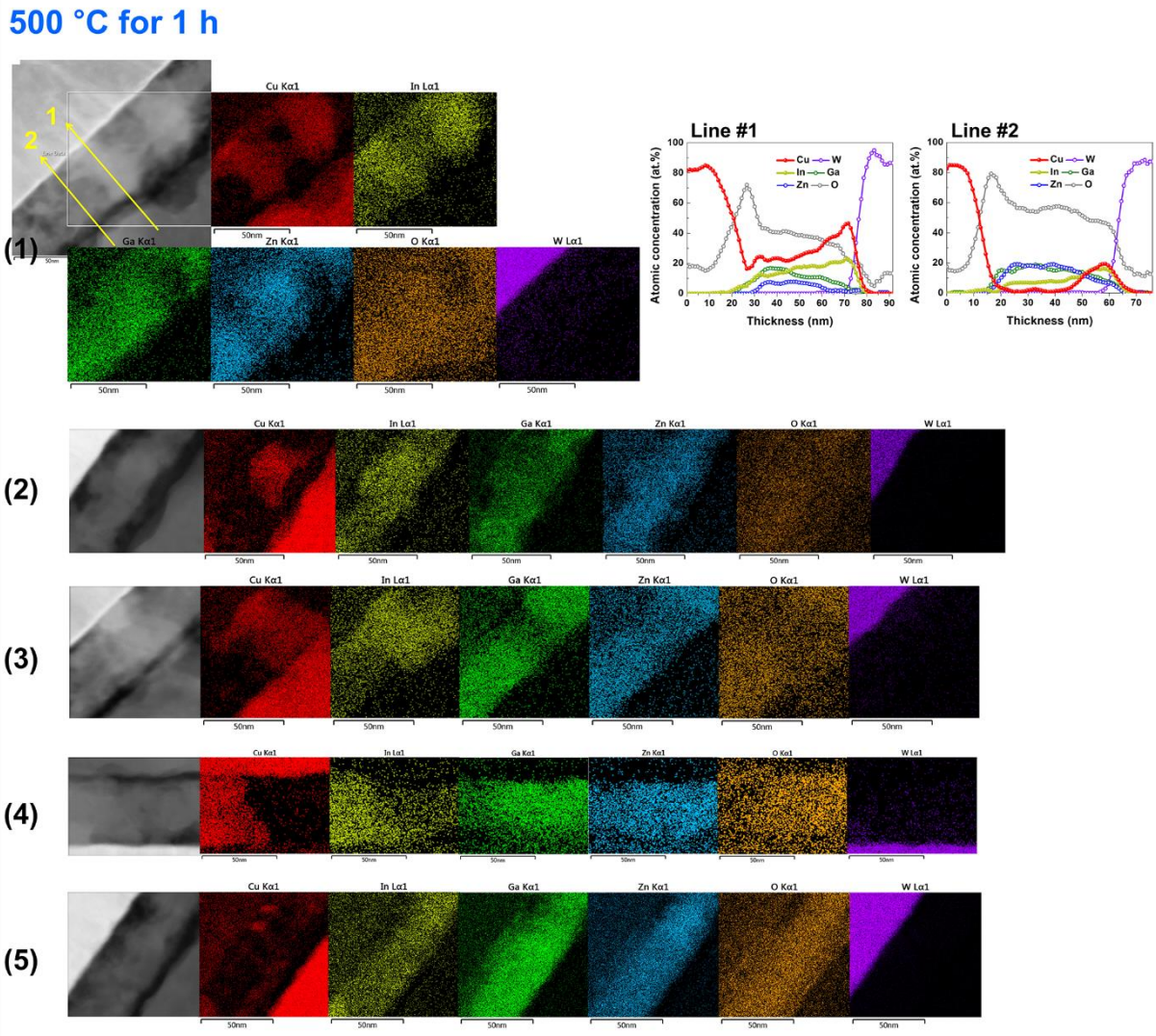

Figure S12. EDS maps and line profiles of the Cu devices after annealing at 500 °C for 1 h, Areas 1-5. In these regions, *In-doped Cu-rich clusters* are dominantly observed.

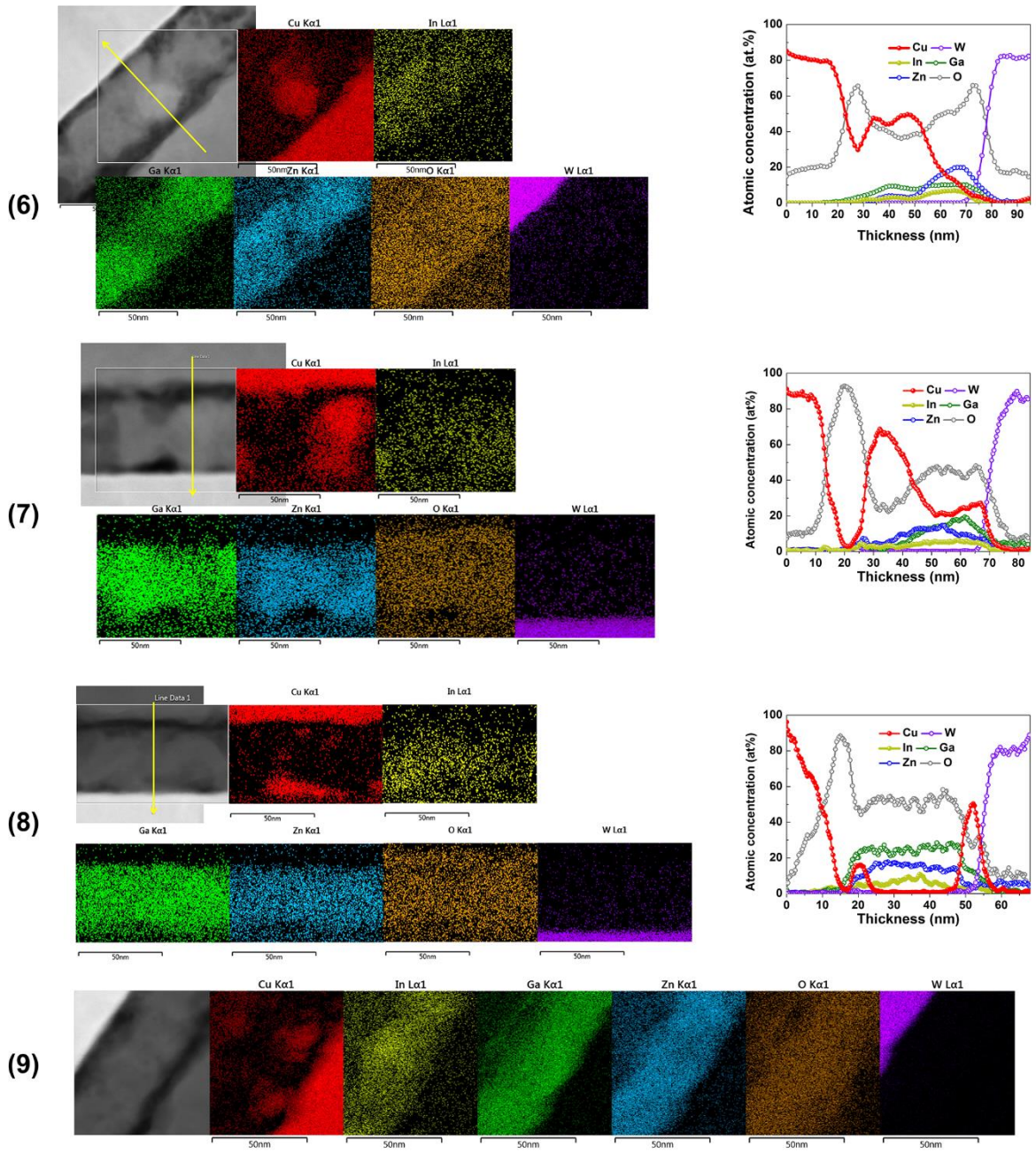

Figure S13. EDS maps and line profiles of the Cu devices after annealing at 500 °C for 1 h, Areas 6-9. In these regions, *In-undoped Cu-rich clusters* are dominantly observed.

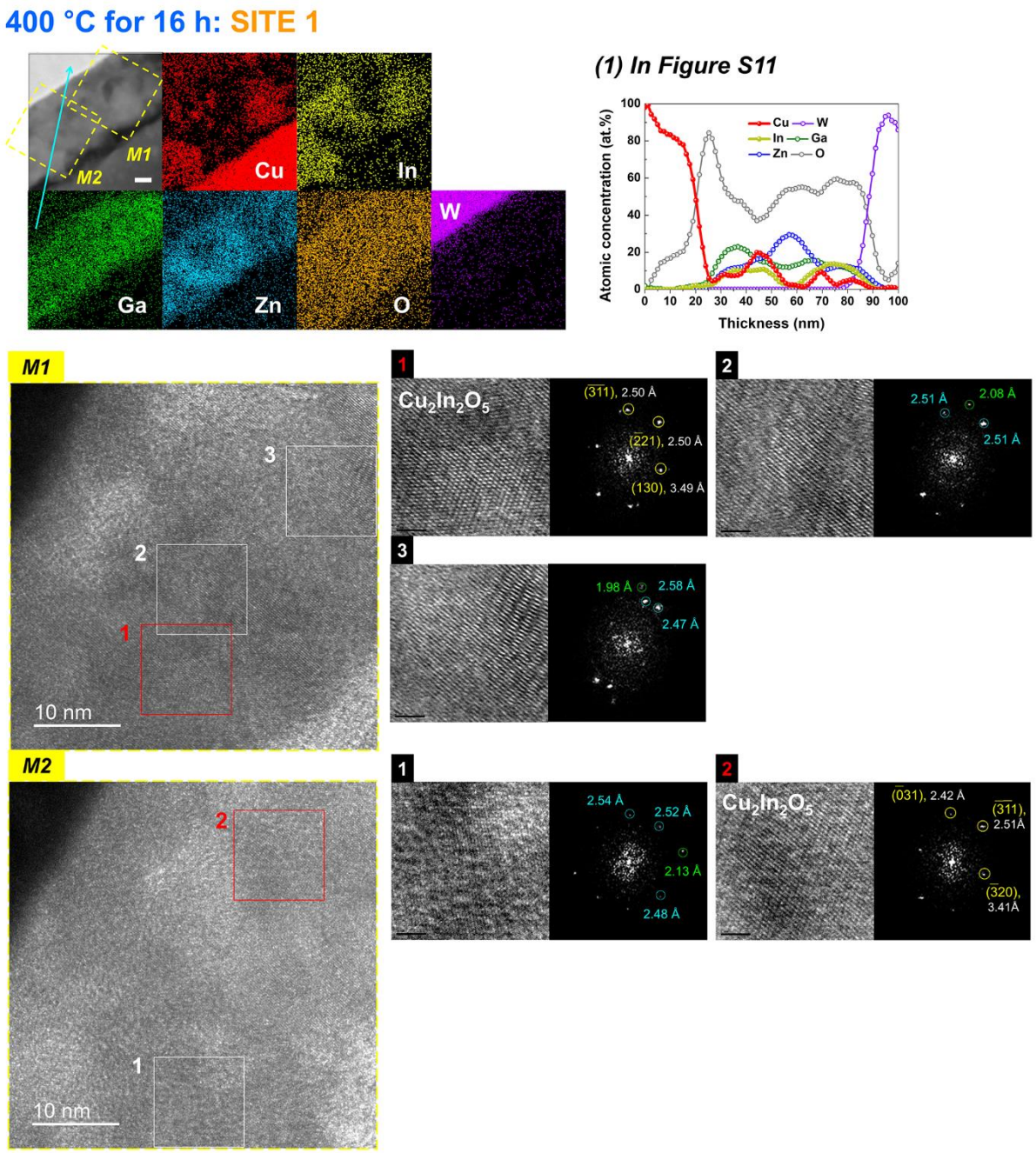

Figure S14. HRTEM images and FFT diffractograms of the Cu devices after annealing at 400 °C for 16 h, SITE 1. The EDS result (1) in Figure S10 was combined with the images. Some images are introduced in Figure 4. Pure Cu was not the dominant crystalline phase because the interplanar spacing of the Cu-rich clusters was wider than the maximum interplanar spacing of pure Cu (2.088 Å, JCPDS 04-0836).

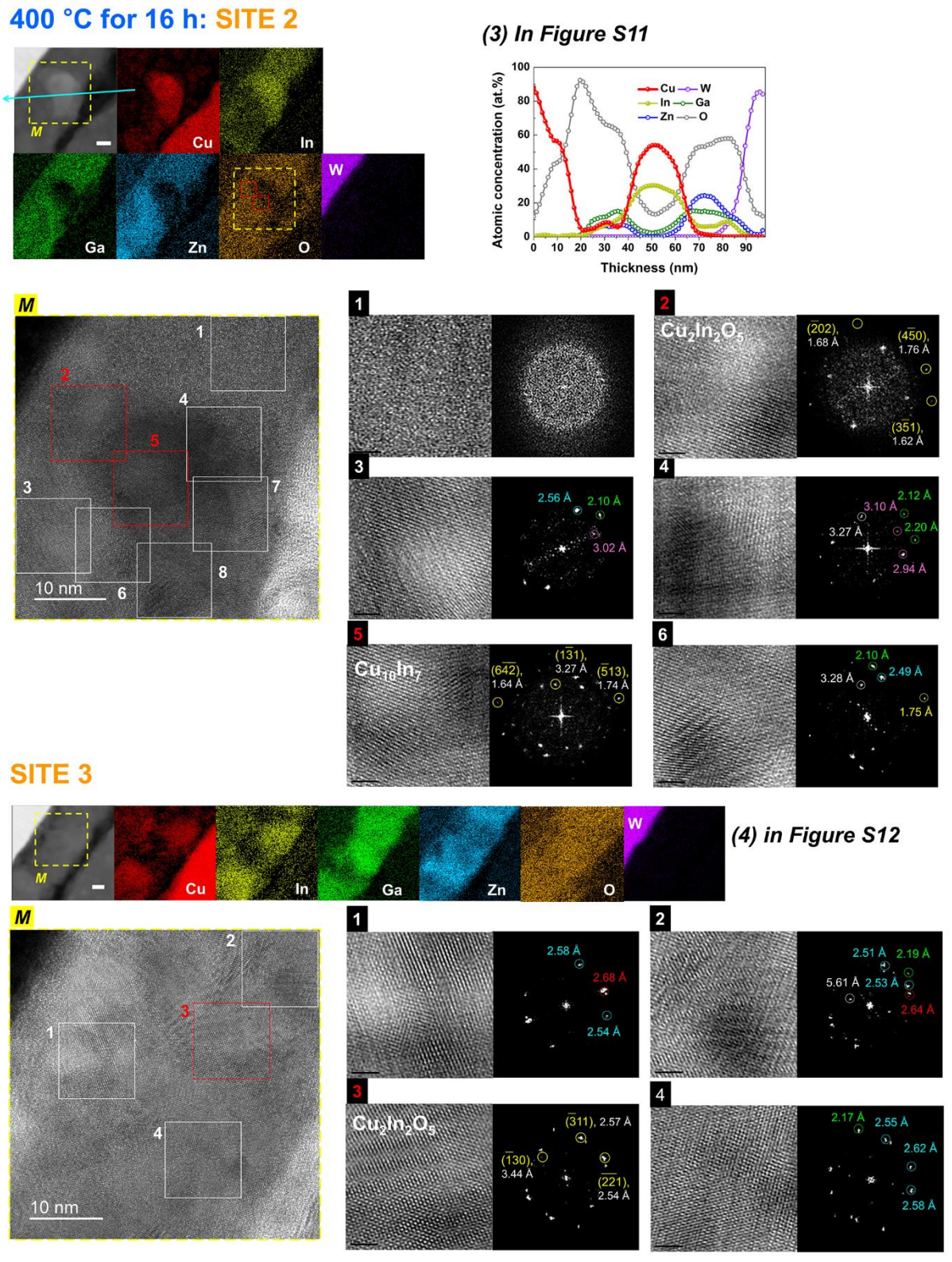

Figure S15. HRTEM images and FFT diffractograms of the Cu devices after annealing at 400 °C for 16 h, SITES 2 and 3. EDS results, (3) in Figure S10 and (4) in Figure S11, were combined with the images of SITES 2 and 3, respectively. Some images are introduced in Figure 4.

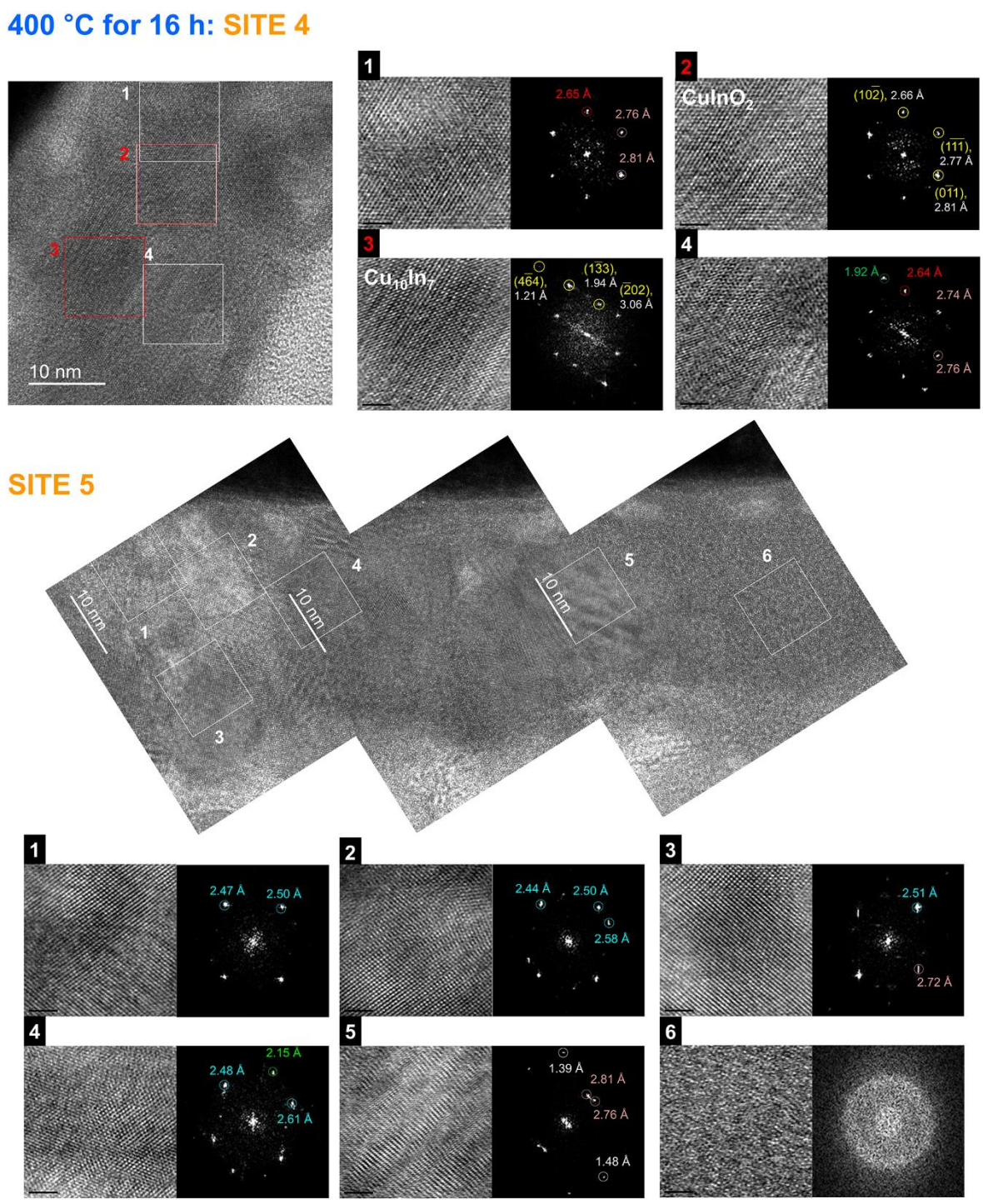

Figure S16. HRTEM images and FFT diffractograms of the Cu devices after annealing at 400 °C for 16 h, SITES 4 and 5. A $CuInO_2$ phase is identified in SITE 4.

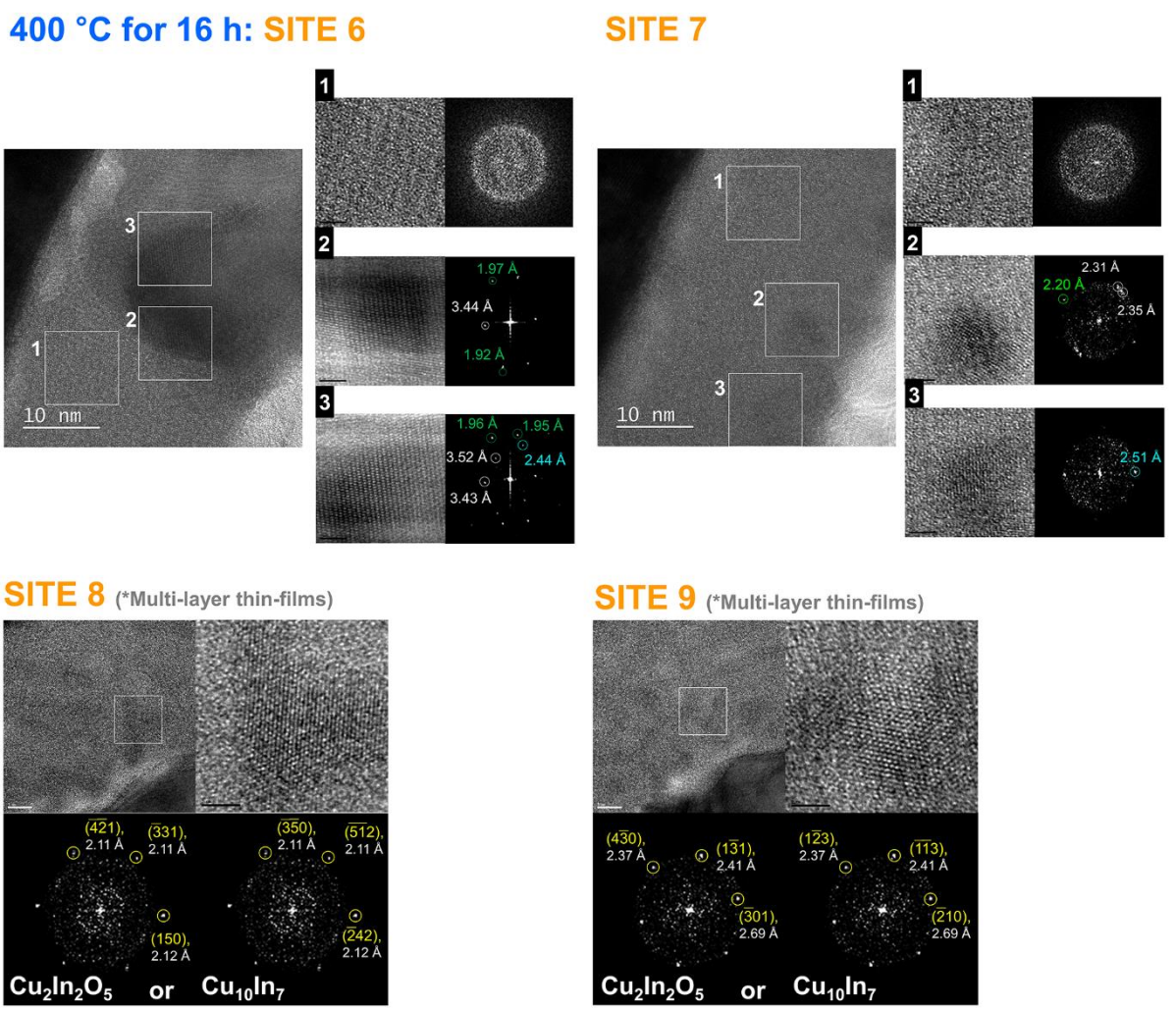

Figure S17. HRTEM images and FFT diffractograms of the Cu devices (SITES 6 and 7) and multi-layer thin films that have the same stacks as the Cu devices (SITES 8 and 9) after annealing at 400 °C for 16 h. Crystalline phases, $Cu_2In_2O_5$ or $Cu_{10}In_7$, are also observed in the multi-layer thin films.

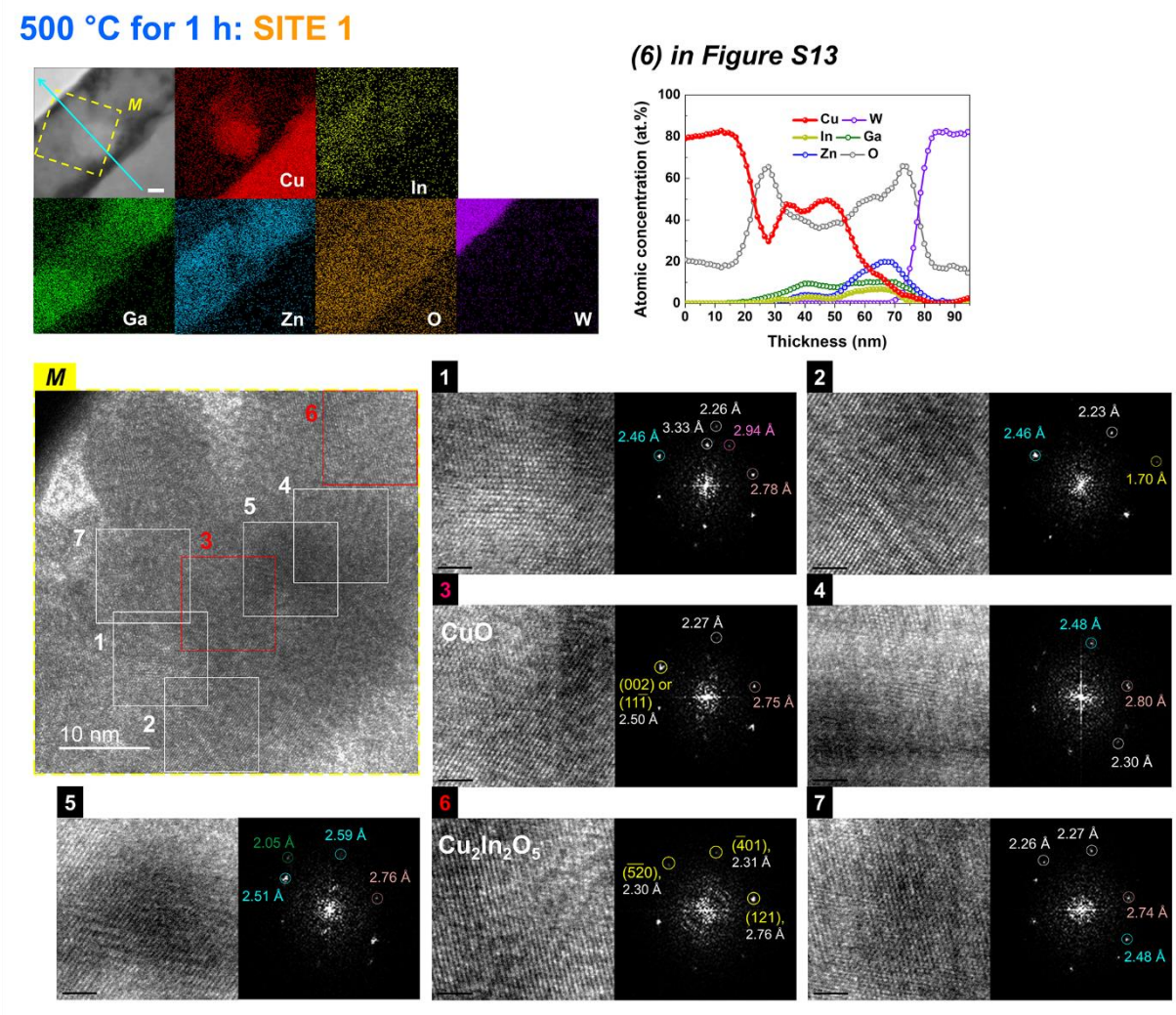

Figure S18. HRTEM images and FFT diffractograms of the Cu devices after annealing at 500 °C for 1 h, SITE 1. An EDS result, (6) in Figure S13, was combined with the images. Some images are introduced in Figure 4.

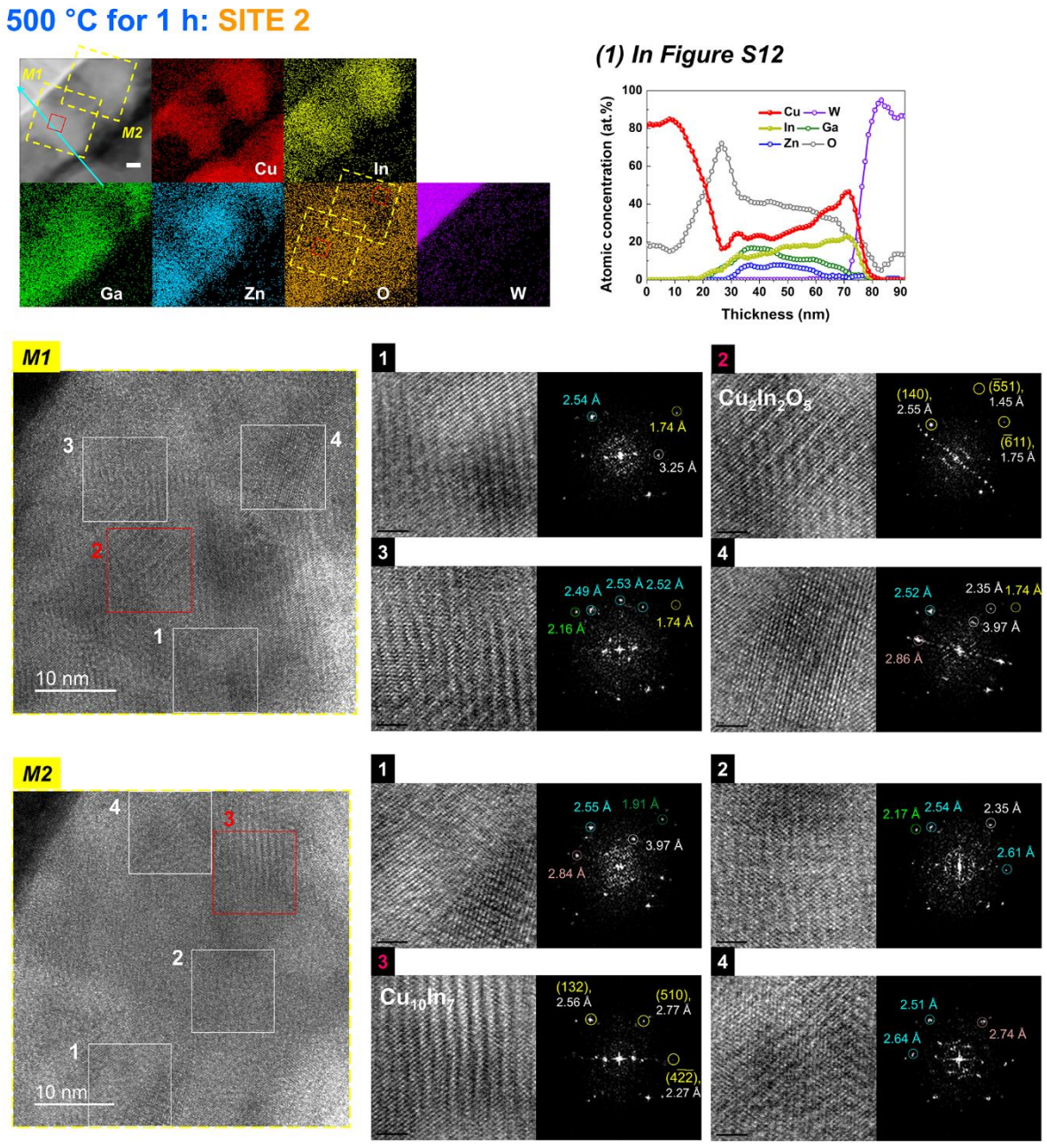

Figure S19. HRTEM images and FFT diffractograms of the Cu devices after annealing at 500 °C for 1 h, SITE 2. An EDS result, (1) in Figure S12, was combined with the images. Some images are introduced in Figure 4.

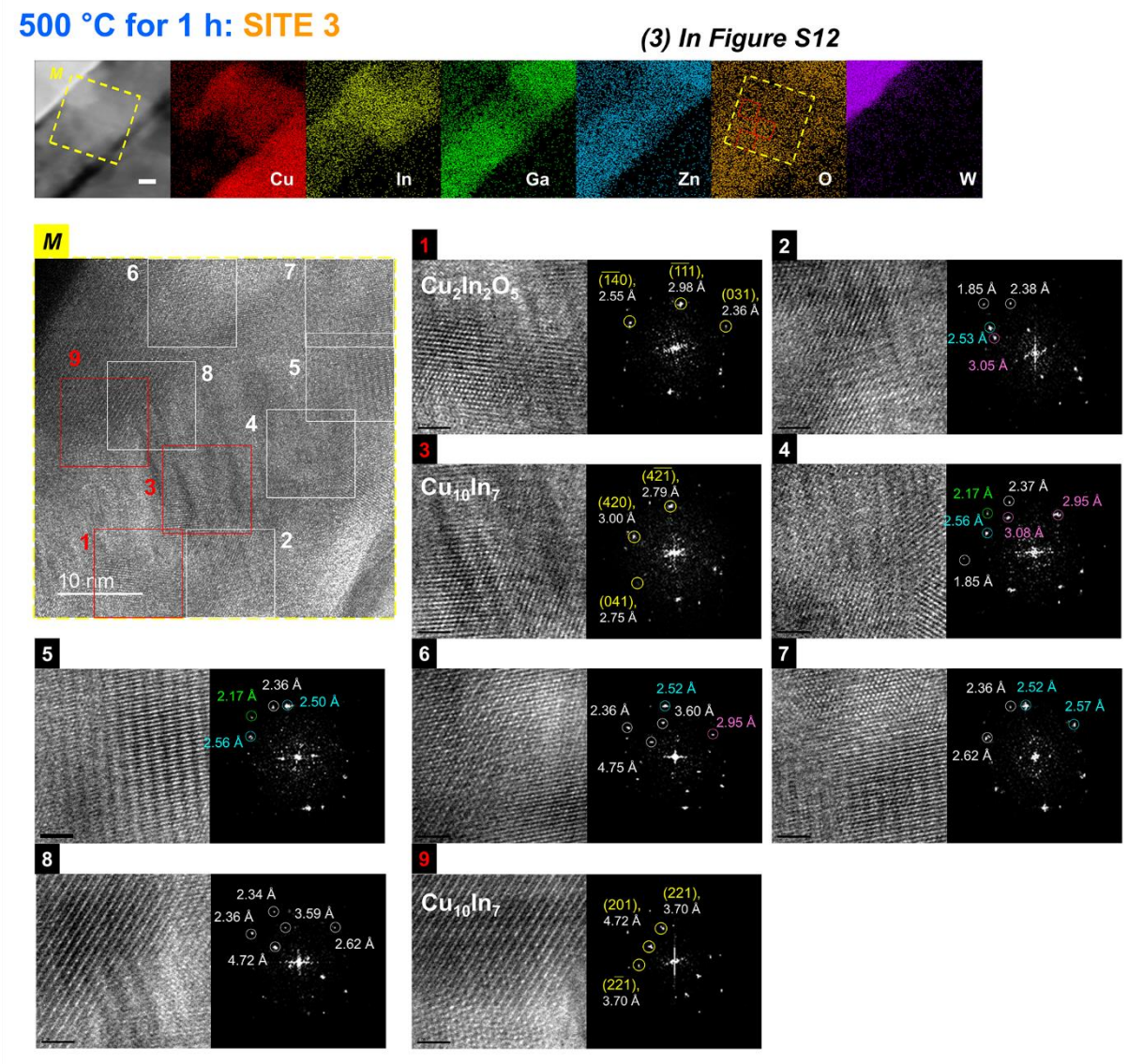

Figure S20. HRTEM images and FFT diffractograms of the Cu devices after annealing at 500 °C for 1 h, SITE 3. An EDS result, (3) in Figure S12, was combined with the images.

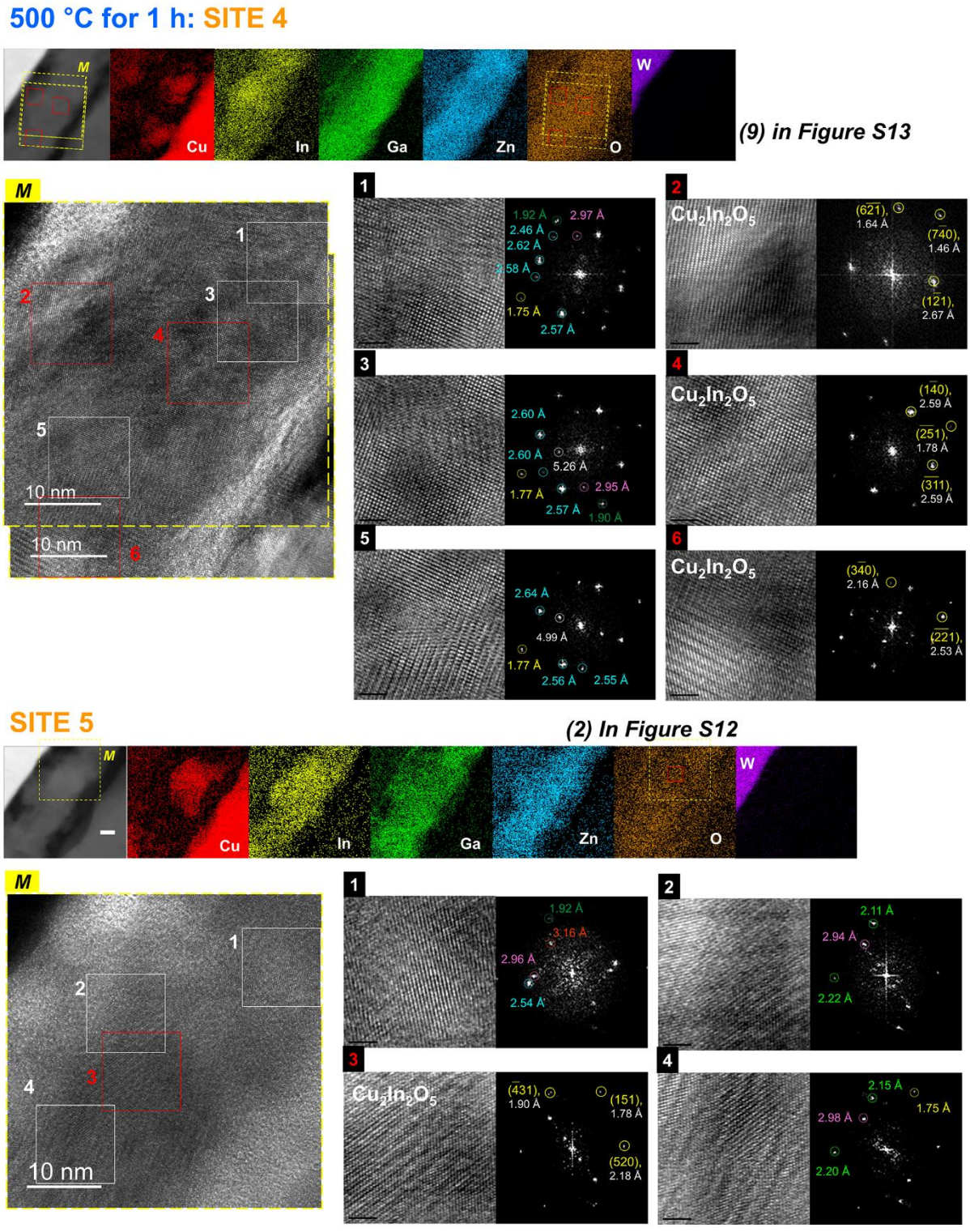

Figure S21. HRTEM images and FFT diffractograms of the Cu devices after annealing at 500 °C for 1 h, SITES 4 and 5. EDS results, (9) in Figure S13 and (2) in Figure S12, were combined with the images of SITES 4 and 7, respectively.

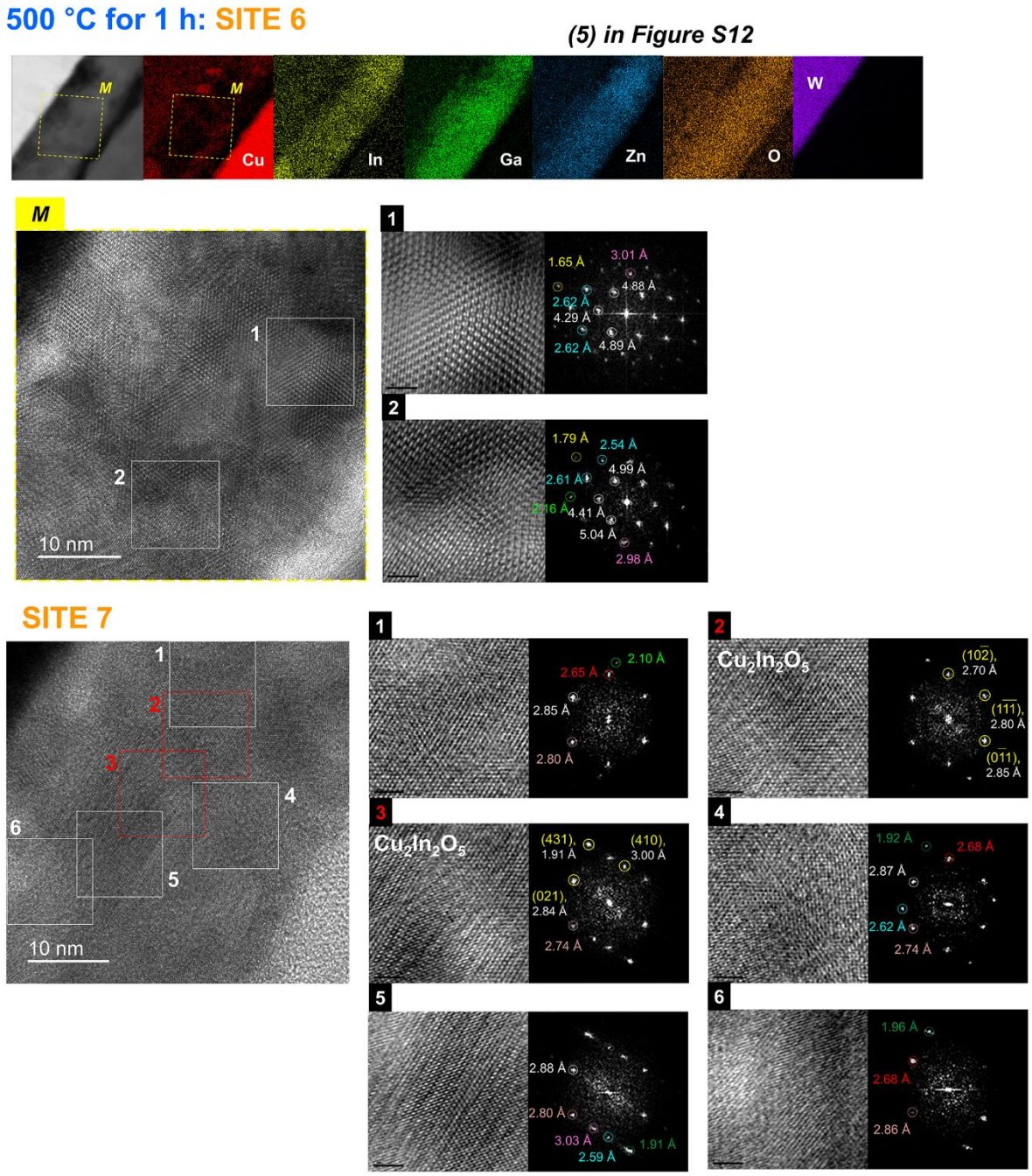

Figure S22. HRTEM images and FFT diffractograms of the Cu devices after annealing at 500 °C for 1 h, SITES 6 and 7. An EDS result, (5) in Figure S12, was combined with the images of SITE 6.

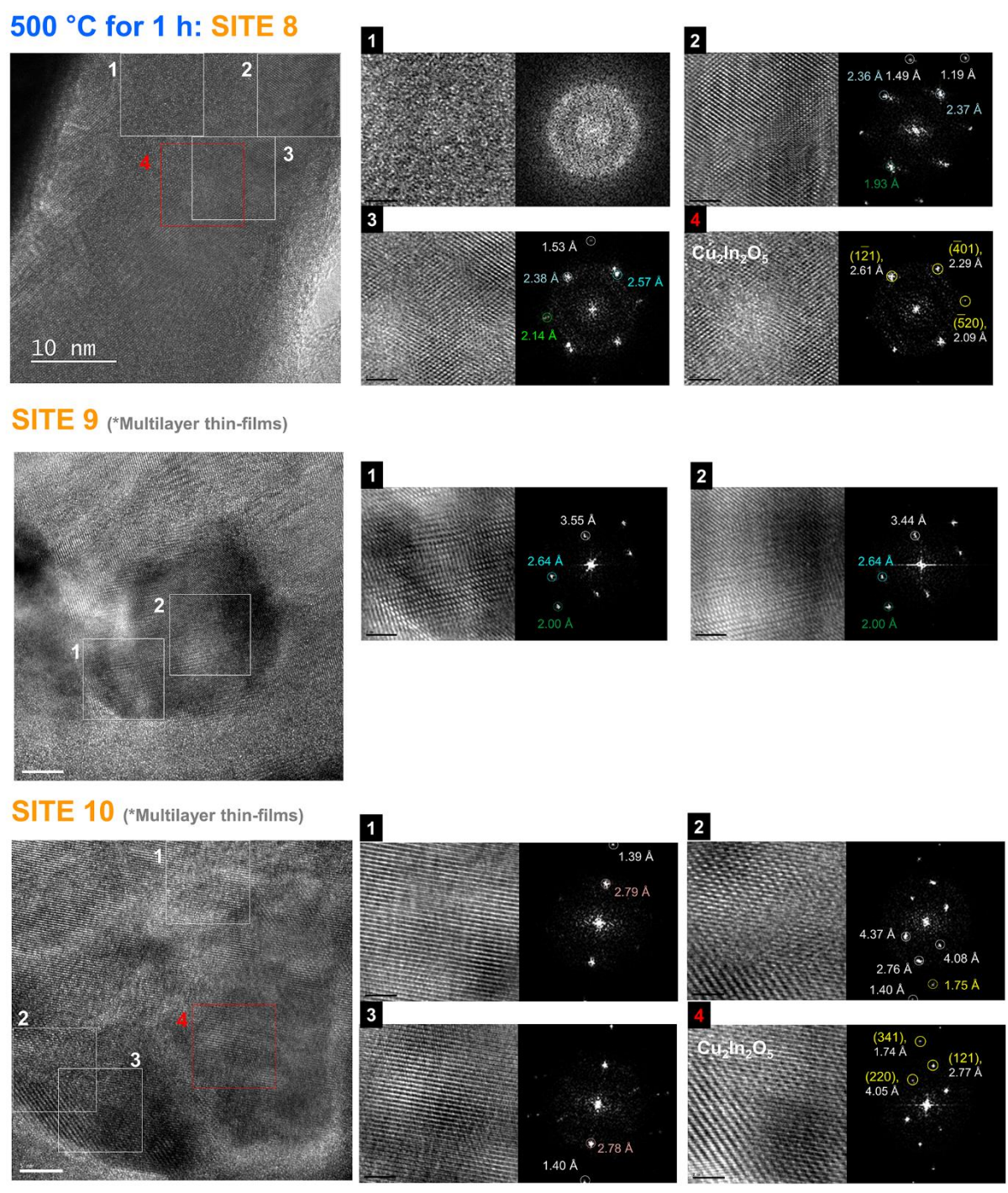

Figure S23. HRTEM images and FFT diffractograms of the Cu devices (SITE 8) and multi-layer thin films that have the same stacks as the Cu devices (SITES 9 and 10) after annealing at 500 °C for 1 h. $Cu_2In_2O_5$ was also identified at multi-layer thin films, as shown in SITE 10.

Secondary ion mass spectrometry (SIMS)

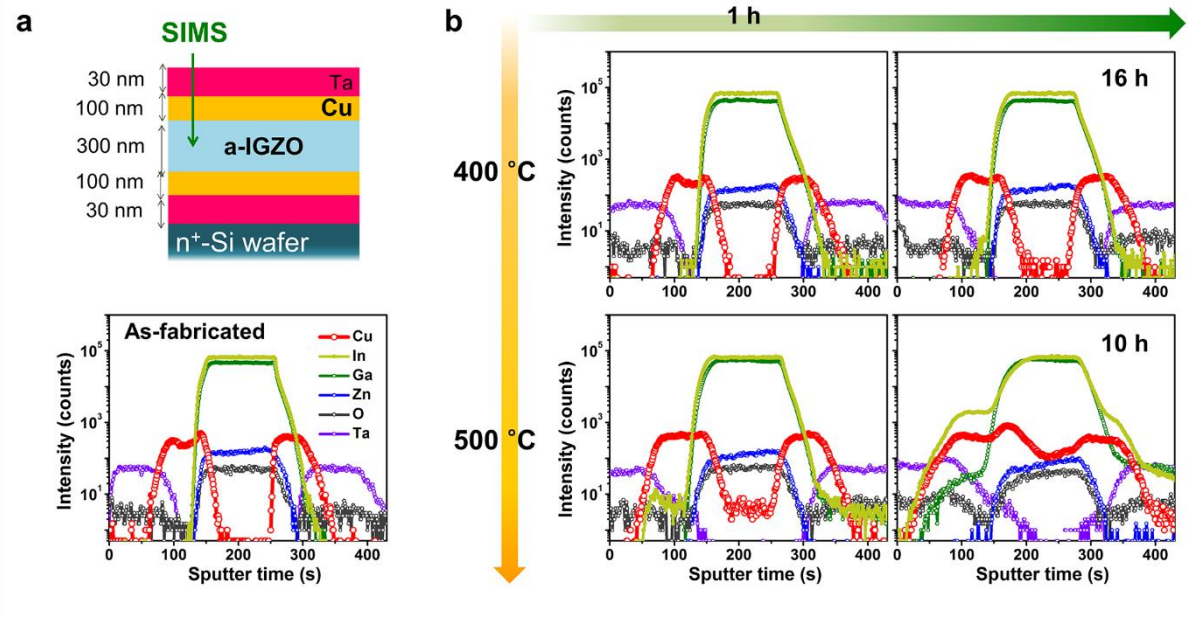

Figure S24. (a) Schematic cross-sectional images of Ta/Cu/a-IGZO/Cu/Ta films and compositional profiles of the films in the as-fabricated state. (b) Composition profile changes of the films with respect to the annealing conditions. Among In, Ga, and Zn in a-IGZO, In predominantly inter-diffused with Cu.

X-ray photoelectron spectroscopy (XPS)

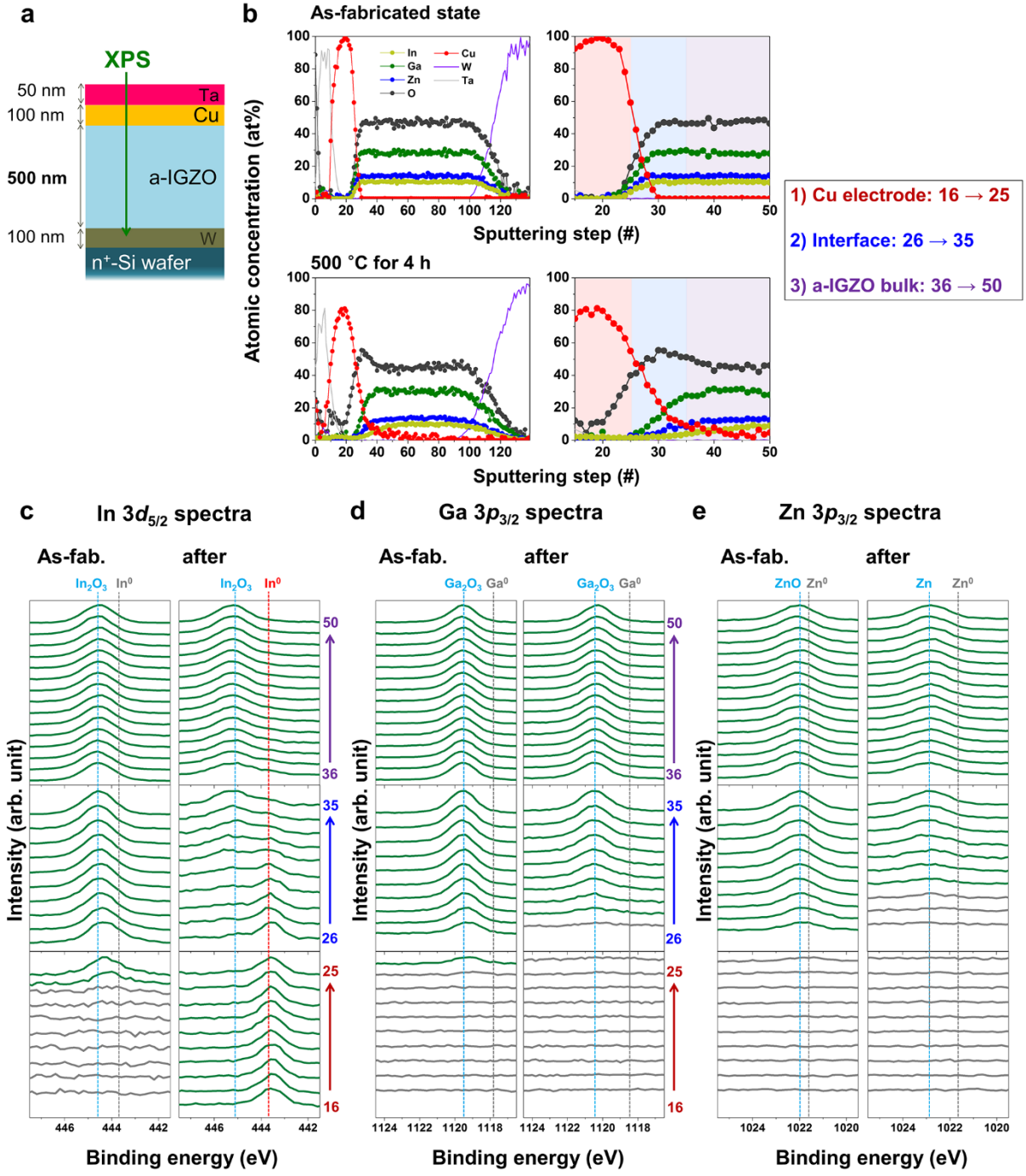

Figure S25. (a) Schematic cross-sectional images of multi-layered Ta/Cu/a-IGZO (500 nm)/ W thin-films. (b) Composition profile changes of the films after annealing at 500 °C for 4 h. T he XPS results of (c) In, (d) Ga, and (e) Zn with respect to the regions, Cu electrode, Cu/a-IG ZO interface, and a-IGZO bulk. The XPS peaks are sited from refs. 50-52.

Figure S25a depicts the schematics of multi-layer thin films that possess the same stacks as the Cu devices. The thickness of the a-IGZO thin films is 500 nm, much thicker than that of the a-IGZO thin-film patches (40 nm) in the devices, to more accurately detect Cu diffusion profiles in a-IGZO. Figure S25b presents the changes in the compositional profiles of the multi-layer thin films after annealing at 500 °C for 4 h, as measured by XPS. After annealing, interdiffusion between Cu and a-IGZO was observed, whereas the diffusion of W into a-IGZO was negligible. Moreover, the concentration of In significantly decreased compared to Ga or Zn, which is clearly observed in the magnified profiles at the Cu/a-IGZO interface. These results are similar to the SIMS results shown in Figure 4d in the main text and Figure S24.

The XPS spectra of In, Ga, Zn, O and Cu with respect to different regions of the thin films, 1) the Cu thin films [step 16 → 25], 2) the Cu/a-IGZO interface [step 26 → 35], and 3) the a-IGZO bulk [step 36 → 50], are presented in Figures S25c-e and S25a-b, respectively. In the In $3d_{5/2}$ spectra, the peak at 444.6 eV corresponding to In_2O_3 was solely observed for the a-IGZO bulk in the as-fabricated state (Figure S27c).[50] However, after annealing, a lower binding energy peak at approximately 443.7 eV, which corresponds to metallic In (In^0), additionally appeared in the Cu thin films and Cu/a-IGZO interface. On the other hand, the XPS spectra of Ga and Zn remained relatively unchanged after annealing compared to In (Figures S25d and S25e).[51,52] These results strongly suggest that Cu dominantly diffuses in a-IGZO by breaking In-O bonds rather than Ga-O or Zn-O bonds, which in turn generates metallic In in a-IGZO (In in the free volume of a-IGZO, In_f) as well as in the Cu thin films. The exsitence of metallic In in Cu-doped a-IGZO also supports the TEM results (Figure 4c in the main text and Figures S10-S23) indicating that intermetallic Cu-In compounds such as $Cu_{10}In_7$ were formed in a-IGZO after annealing. The intensity of the In^0 peak was diminished as the distance

between the Cu and a-IGZO thin films increased, which confirms that In^0 in a-IGZO was induced by substitutional Cu diffusion.

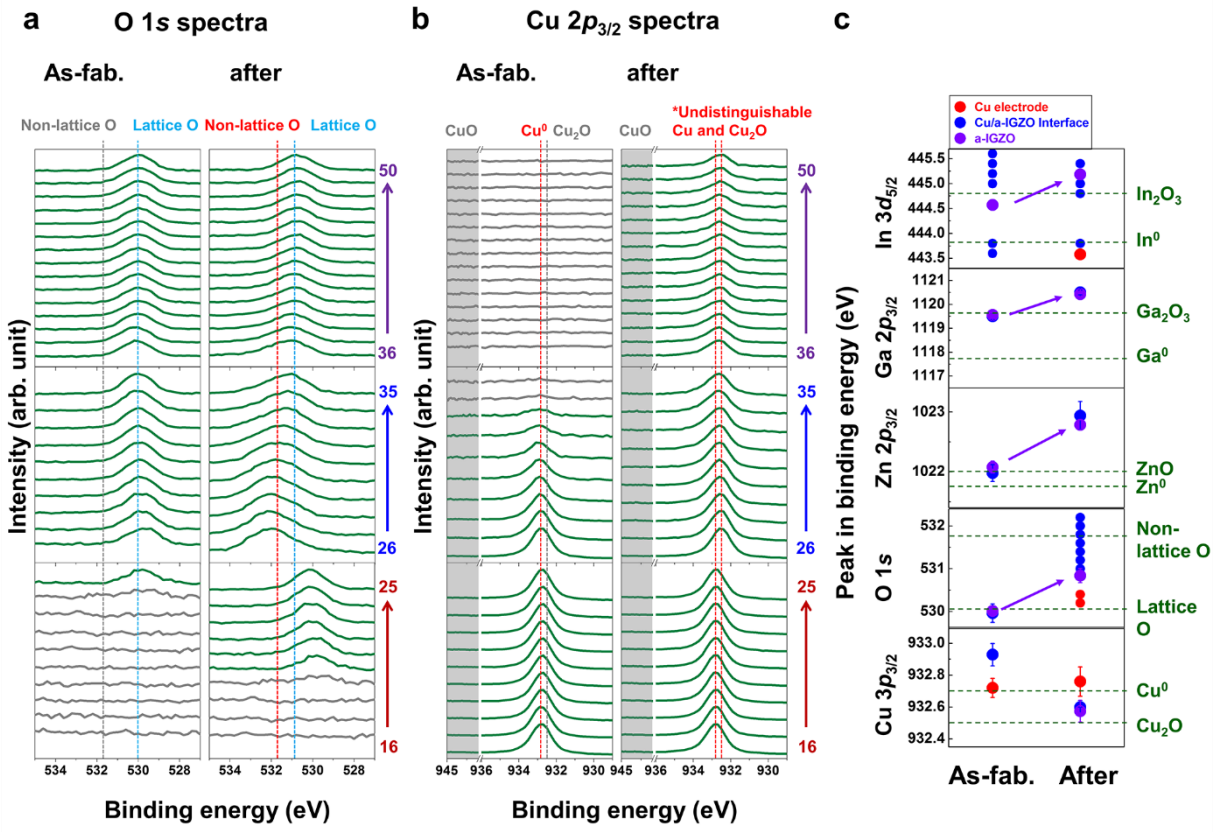

Figure S26. The XPS results of (a) O and (b) Cu with respect to the regions, Cu electrode, Cu/a-IGZO interface, and a-IGZO bulk. The XPS peaks are sited from refs. 53-56. (g) The value of the XPS peak shift of the elements after annealing at 500 °C for 4 h.

In the O 1*s* spectra (Figure S26a) obtained in the as-fabricated state, the peak at 530 eV corresponding to lattice oxygen bonding was dominantly observed for the a-IGZO thin films but for the Cu thin films. After annealing, the main peak in the a-IGZO bulk was nearly unchanged, whereas a peak at ~532 eV, assignable to non-lattice oxygen bonding, such as O ions that are in O-deficient regions within a-IGZO[53,54] and/or weakly bound O species (e.g., H_2O, CO_2),[55] was newly observed at the Cu/a-IGZO interface. These results may be induced that partial interface delamination between Cu and a-IGZO thin films occurs after annealing at

500 °C, as shown in the TEM images (Figure 4a in the main text and Figures S12 and S13), resulting in the formation of unbonded oxygen molecules.

In the Cu 2$p_{3/2}$ spectra (Figure S26b) obtained in the as-fabricated state, a peak can be observed from the Cu thin films to the middle of the Cu/a-IGZO interface. The dominant XPS peak is located at 932.7 eV, indicating the presence of metallic Cu.[56]

Afer annealing, ~932.7 eV peak is newly detected at a-IGZO bulk. Satelite peaks in the range of 940-945 eV and the peak at ~933.7 eV, which are a sign of the existence of Cu^{2+}-based oxides (e.g., CuO, $Cu_2In_2O_5$), were not observed.[56] These results appear to be contradictory to the TEM results indication that (1) Cu^0 (metallic Cu, Cu-In intermetallic compounds) was negligible compared to Cu oxides and (2) the $Cu_2In_2O_5$ phase (Cu^{2+}-based oxides) was frequently identified. However, two factors should be considered as follows.

First, the peak of In_2O_3, Ga_2O_3, and ZnO in a-IGZO bulk and Cu/a-IGZO interface is positively shifted after annealing although the spectral shape was nearly constant, as shown in Figure S26c. The peak shift of elements has been observed when the surrounding bonding conditions are changed.[57,58] Thus, the formation of Cu-rich clusters would the change initial bonding nature of a-IGZO and induce a positive shift of the XPS peaks of the elements. Similary, the XPS peak of Cu in a-IGZO, as dispersed phases, would be positively shifted compared to the bulk state. Cu^+-based oxides (Cu_2O, $CuInO_2$) in the bulk state have dominant XPS peak as 932.5 eV with similar spectra shapes to Cu^0. Therefore, we believe the dominant chemical state of Cu in a-IGZO is Cu^+, for which the XPS peak is positively shifted to 932.7 eV.

Lastly, $CuInO_2$ is thermodynamically unstable compared to $Cu_2In_2O_5$.[59] It is possible that the $CuInO_2$ clusters were oxidized to $Cu_2In_2O_5$ during fabrication of the TEM samples (e.g., focused-ion beam milling) and/or the O_2 plasma cleaning processes to eliminate organic contaminants on the TEM samples. Although we speculate that the frequent detection of the $Cu_2In_2O_5$ phase compared to the $CuInO_2$ phase was induced by additional oxidation of

$CuInO_2$ clusters, further studies are needed to unravel the exact cause of the discrepancies between the XPS and TEM results. However, we believe that the important message of this study is that Cu dopant acts as a crystallization seed in a-IGZO and forms heterogeneous Cu-In-O clusters, In-doped Cu oxides and Cu-In intermetallic compounds in a-IGZO that could be delivered without identification of the dominant crystalline phase of In-doped Cu oxide clusters, whether $CuInO_2$ or $Cu_2In_2O_5$.

For more clear indentification of dominant chemical state of Cu in a-IGZO, AES anaylsis were conducted on the same multi-layer thin-films and the coressponding results are presented in Figure S29.

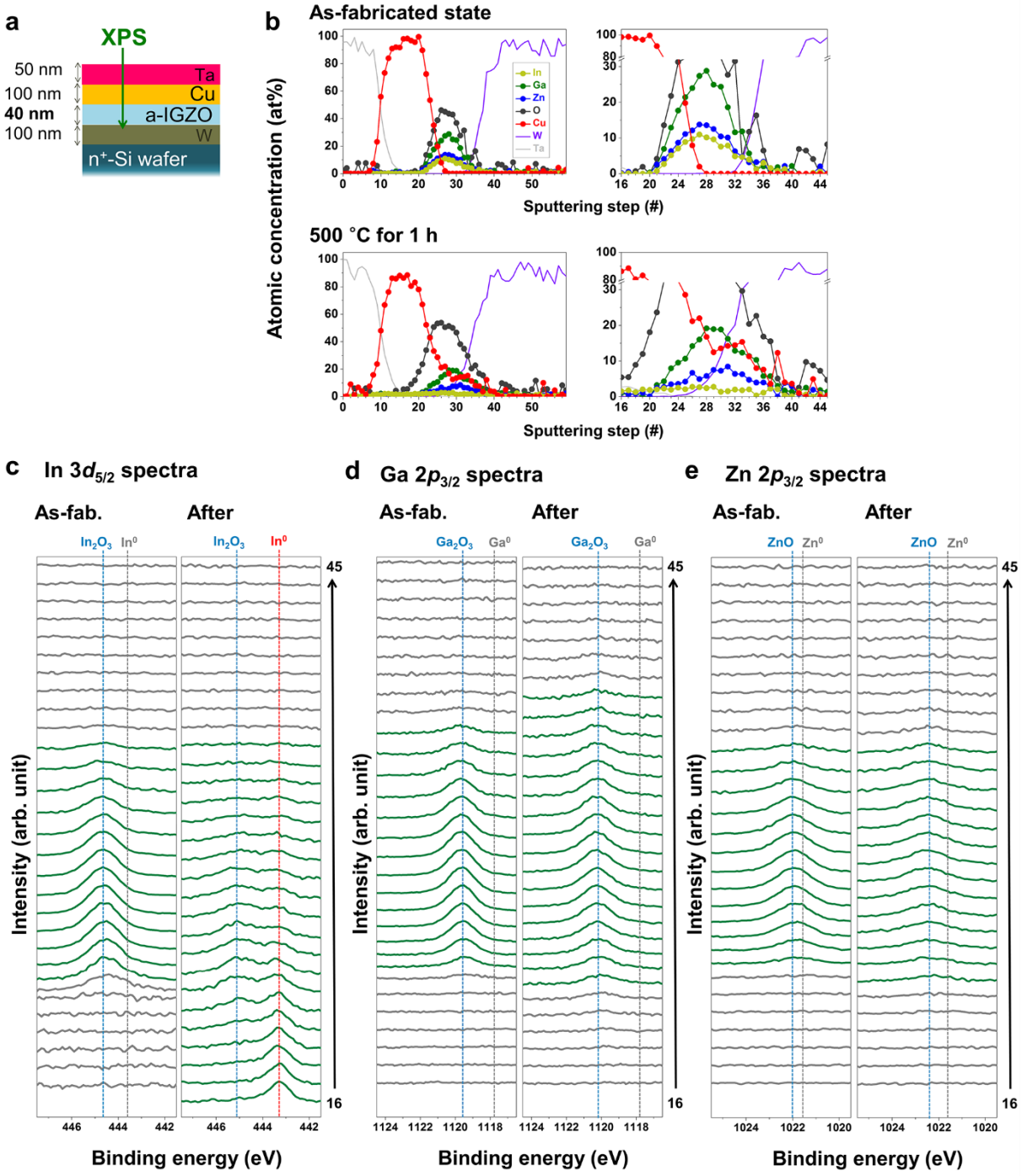

Figure S27. (a) Schematic cross-sectional images of multi-layered Ta/Cu/a-IGZO (40 nm)/W thin-films. (b) Composition profile changes of the films after annealing at 500 °C for 1 h. The XPS results of (c) In, (d) Ga, and (e) Zn with respect to the sputtering step from 16 to 45. The XPS peaks are sited from refs. 50-52.

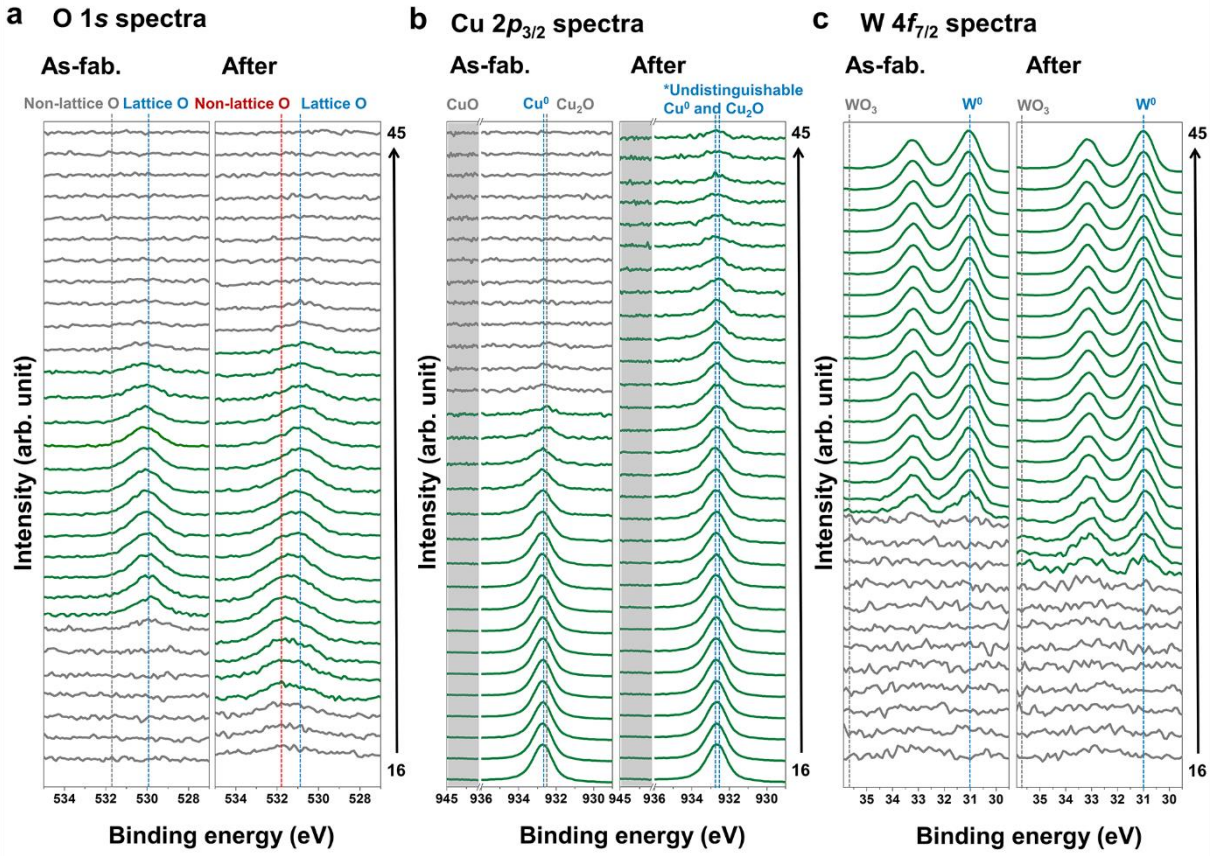

Figure S28. The XPS results of (a) O, (b) Cu, and (c) W with respect to the sputtering depth f rom 16 to 45. The XPS peaks are sited from refs. 53-56,60,61.

Figures S27 and S28 present the XPS analysis of multi-layer thin films that possess the same stacks and same thicknesses (40-nm-thick a-IGZO thin films) as the Cu devices. Although the thickness of the a-IGZO thin films was changed from 500 nm to 40 nm and the annealing time decreased from 4 h to 1 h, changes in the compositional profiles and the chemical state of the elements showed similar results. In the as-fabricated state, the W $4f_{7/2}$ spectra revealed that the dominant chemical state of W-BE is metallic W^0, and oxidized W (WO_x, WO_3) and nitrated W (WN_y) were not detected.[60,61] Furthermore, after annealing at 500 °C for 1 h, the dominant chemical state of W was nearly unchanged, as in the previous study.[14]

Auger electron spectroscopy (AES)

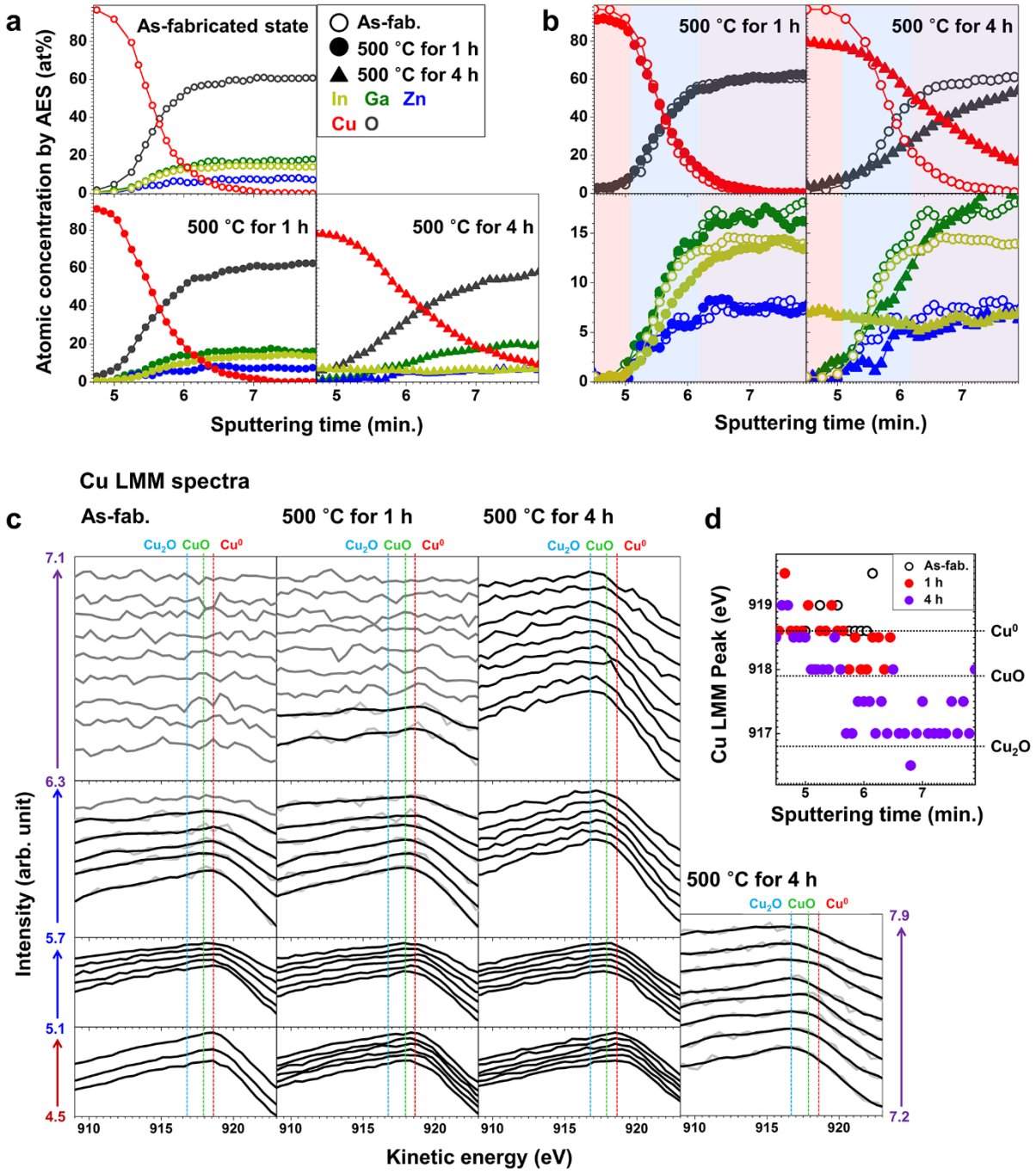

Figure S29. (a) Composition profile changes of multi-layer films as depicted in Figure S25a after annealing at 500 °C for 1-4 h. (b) Maginified composition profile in the vicinity of Cu/a-IGZO interfaces. (c) Cu LMM spectra with respect to the sputtering time from 4 to 7.2 minut s. Cu LMM peak positions in metallic Cu^0, Cu^+, and Cu^{2+} are sited from ref. 62. (d) The chan ges of Cu LMM peak with respect to sputtering time.

Figure S29a presents the changes in the composition profile of multi-layer thin-films (Figure S25a) after annealing at 500 °C for 1-4 h. As the annealing time increased, substantial

Cu diffusion into a-IGZO occurred. Interestingly, the AES results also revealed that the In concentration decreased siginificantly compared to Ga and Zn, supporting In as the dominant substitution site of Cu (Figure S29b) and thus, corroborating the results of SIMS and XPS. Note that the stoichiometry of In, Ga, and Zn in a-IGZO (In:Ga:Zn=1:1.2:0.5) was different from the results of XPS analysis, although the same multi-layer thin films were used for the analysis. This discrepancy may be due to the different instruments and the different energy ranges used to extract the atomic concnetrations of elements.

Figure S29c presents the Cu LMM spectra of multi-layer films for different sputtering times, and the corresponding peak is plotted in Figure S29d. Regardless of annealing, the chemical state of Cu thin films was not changed from metallic Cu (~918.6 eV).[62] However, the LMM peak of Cu in a-IGZO decreased to ~917 eV. These results may indicate that the dominant chemical state of Cu in a-IGZO is Cu^{+} [62] and Cu^{+}-based *p*-type oxides such as Cu_2O and $CuInO_2$ were dominantly formed in a-IGZO, which is consistent with the speculation based on the Cu $2p_{3/2}$ spectra. Note that the AES peak of Cu in a-IGZO, as a dispersed phase, has the potential to be negatively shifted compared to the bulk state, in contrast to the case of XPS analysis.[58] If a negative peak shift occurred in the Cu LMM spectra, metallic Cu or Cu^{2+} (917.9 eV) would be the dominant phase of Cu in a-IGZO.[62] It is obvious that metallic Cu is not the dominant phase of the Cu-rich clusters, because the formation of Cu-rich clusters decreases the G of the Cu devices, and the spatial gaps among the Cu-rich clusters are narrow enough to form ohmic conduction if the Cu-rich clusters were metallic phases (Figure 4a in the main text and Figures S10-23). Unravelling the exact chemical state of Cu in a-IGZO, whether Cu^{+} or Cu^{2+}, will be one of the topics for further research.

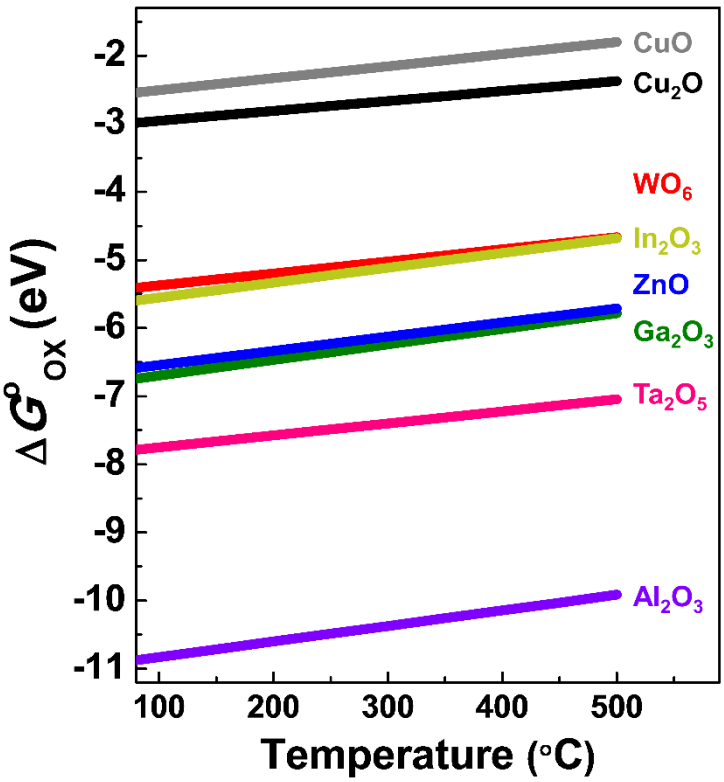

Figure S30. Standard Gibbs free energy of oxide formation (ΔG°_{OX}) of metals which used for the fabrication of the Cu devices and W devices.[63]

Table S2. Estimation of the atomic concentration in Cu and In-Ga-Zn-O thin films from the molar mass and density.

	Crystal Structure	Molar mass [g mol^{-1}]	Density [g cm^{-3}]	**Concentration [cm^{-3}]**	Ref.
Cu	FCC	63.55	8.94	**8.47×10^{22}**	64
$InGaZnO_4$	$R\bar{3}m$	44.85	6.38	8.56×10^{22}	65,66
a-IGZO in this study[a)]			~5.8	**~7.78×10^{22}**	14

[a)]Sputtering target was polycrystalline $InGaZnO_4$. Each concentration of In, Ga, or Zn is ~10^{22} cm^{-3}.

Table S3. Size variations of the elements with respect to the valence state.[67,68]

Valence state	Radius [Å]					
	In	Ga	Zn	O	Cu	W
2^-				1.26		
0 (atom)	1.55	1.30	1.35	0.60	1.35	1.35
1^+					0.91	
2^+			0.88		0.87	
3^+	0.94	0.76				

References for Supporting Information

[1] S. M. Sze, D. C. Mattis, *Physics of Semiconductor Devices*, John Willey & Sons, Inc., New York, USA, **1981**.

[2] L. J. Brillson, Y. Lu, *J. Appl. Phys.* **2011**, 109, 121301.

[3] T.-C. Fung, C.-S. Chuang, C. Chen, K. Abe, R. Cottle, M. Townsend, H. Kumomi, J. K anicki, *J. Appl. Phys*. **2009**, 106, 084511.

[4] D. K. Schroder, *Semiconductor Material and Device Characterization*, John Wiley & Sons, Inc., Hoboken, New Jersey, USA, **2006**.

[5] H. B. Michaelson, *J. Appl. Phys.* **1977**, 48, 4729.

[6] A. Chasin, S. Steudel, K. Myny, M. Nag, T.-H. Ke, S. Schols, J. Genoe, G. Gielen, P. Heremans, *Appl. Phys. Lett.* **2012**, 101, 113505.

[7] J. Zhang, Y. Li, B. Zhang, H. Wang, Q. Xin, A. Song, *Nat. Commun.* **2015**, 6, 7561.

[8] C.-F. Huang, B.-Y. Tsui, C.-H. Lu, *Jpn. J. Appl. Phys.* **2008**, 47, 872.

[9] J. Meyer, S. Hamwi, M. Kröger, W. Kowalsky, T. Riedl, A. Kahan, *Adv. Mater.* **2012**, 2 4, 5408.

[10] D. H. Lee, K. Nomura, T. Kamiya, H. Hosono, *IEEE Electron Device Lett.* **2011**, 32, 1695.

[11] B. Psiuk, J. Szade., H. Schroeder, H. Haselier, M. Mlynarczyk, R. Waser, K. Szot, *App l. Phys. A: Mater. Sci. Process* **2007**, 89, 451.

[12] A. Chasin, M. Nag, A. Bhoolokam, K. Myny, S. Steudel, S. Schols, J. Genoe, G. Giele n, P. Heremans, *IEEE Trans. Electron Devices* **2013**, 60, 3407.

[13] J. E. Medvedeva, C. L. Hettiarachchi, *Phys. Rev. B* **2010**, 81, 125116.

[14] H.-W. Yeon, S.-M. Lim, J.-K. Jung, H. Yoo, Y.-J. Lee, H.-Y. Kang, Y.-J. Park, M. Ki m, Y.-C. Joo, *NPG Asia Mater.* **2016**, 8, e250.

[15] R. F. Pierret, *Semiconductor Device Fundamentals*, Addison-Wesley, New York, USA, **1996**.

[16] A. I. Taub, F. Spapen, *Acta Metall.* **1980**, 28, 1781.

[17] S. Torquato, *Nature* **2000**, 405, 521.

[18] J. Bang, G.-Q. Lu, *J. Mater. Res.* **1995**, 10, 1321.

[19] J. Maier, *Solid State Ionics* **2004**, 175, 7.

[20] J. R. Yeargan, H. L. Taylor, *J. Appl. Phys.* **1968**, 39, 5600.

[21] G. A. N. Connel, D. L. Camphausen, W. Paul, *Philos. Mag.* **1972**, 26, 541.

[22] H.-J. Chung, J. H. Jeong, T. K. Ahn, H. J. Lee, M. Kim, K. Jun, J.-S. Park, J. K. Jeong, Y.-G. Mo, H. D. Kim, *Electrochem. Solid-State Lee.* **2008**, 11, H51.

[23] M.-C. Chen, T.-C. Chang, C.-T. Tsai, S.-Y. Huang, S.-C. Chen, C.-W. Hu, S. M. Sze, M.-J. Tsai, *Appl. Phys. Lett.* **2010**, 96, 262110.

[24] C. H. Kim, Y. H. Jang, H. J. Hwang, C. H. Song, Y. S. Yang, J. H. Cho, *Appl. Phys. Lett.* **2010**, 97, 062109.

[25] M.-C. Chen, T.-C. Chang, S.-Y. Huang, S.-C. Chen, C.-W. Hu, C.-T. Tsai, S. M. Sze, *Electrochem. Solid-State Lett.* **2010**, 13, H191.

[26] M.-C. Chen, T.-C. Chang, S.-Y. Huang, G.-C. Chang, S.-C. Chen, H.-C. Huang, C.-W. Hu, S. M. Sze, T.-M. Tsai, D.-S. Gan, F.-S. Yeh, M.-J. Tsai. *Electrochem. Solid-State Lett.* **2011,** 14, H475.

[27] Z. Q. Wang, H. Y. Xu, X. H. Li, X. T. Zhang, Y. X. Liu, Y. C. Liu, *IEEE Electron De vice Lett.* **2011**, 32, 1442.

[28] Z. Q. Wang, H. Y. Xu, X. H. Li, H. Yu, Y. C. Liu, X. J. Zhu, *Adv. Funct. Mater.* **2012**, 22, 2759.

[29] M.-S. Kim, Y. H. Hwang, S. Kim, Z. Guo, D.-I. Moon, J.-M. Choi, M.-L. Seol, B.-S. B ae, Y.-K. Choi, *Appl. Phys. Lett.* **2012**, 101, 243503.

[30] Y.-S. Fan, P.-T. Liu, C.-H. Hsu, *Thin Solid Films* **2013**, 549, 54.

[31] W. Hu, L. Zou, X. Chen, N. Qin, S. Li, D. Bao, *ACS Appl. Mater. Interfaces* **2014**, 6, 5 012.

[32] H. K. Li, T. P. Chen, S. G. Hu, W. L. Lee, Y. Liu, Q. Zhang, P. S. Lee, X. P. Wang, H. Y. Li, G.-Q. Lo, *ECS J. Solid State Sci. Technol.* **2016**, 5, Q239.

[33] Q. Li, Y. Li, L. Gao, F. Ma, Z. Song, K. Xu, *RSC Adv.* **2016**, 6, 42347.

[34] Y. Pei, B. Mai, X. Zhang, R. Hu, Y. Li, Z. Chen, B. Fan, J. Liang, G. Wang, *J. Electro n. Mater.* **2015**, 44, 645.

[35] Y. Pei, B. Mai, X. Zhang, R. Hu, Y. Li, Z. Chen, B. Fan, J. Liang, G. Wang, *Curr. App l. Phys.* **2015**, 15, 441.

[36] R. Degraeve, B. Kaczer, G. Groeseneken, *Microelectron. Reliab.* **1999**, 39, 1445.

[37] S. C. Chae, J. S. Lee, S. Kim, S. B. Lee, S. H. Chang, C. Liu, B. Kahng, H. Shin, D.-W. Kim, C. U. Jung, S. Seo, M.-J. Lee, T. W. Noh, *Adv. Mater.* **2008**, 20, 1154.

[38] R. Waser, R. Dittmann, C. Staikov, K. Szot, *Adv. Mater.* **2009**, 21, 2632.

[39] K. Okada, *Jpn. J. Appl. Phys.* **1997**, 36, 1443.

[40] Y.-L. Cheng, Y.-L. Chang, C.-Y. Hsieh, J.-R. Lin, *ECS J Solid State Sci. Technol.* **2013**, 2, N125.

[41] A. Bid, A. Bora, A. K. Raychaudhuri, *Phys. Rev. B* **2006**, 74, 035426.

[41] H. Hosono, *J. Non-cryst. Solids* **2006**, 352, 851.

[42] T. Kamiya, K. Nomura, H. Hosono, *J. Disp. Technol.* **2009**, 5, 273.

[43] F. Funabiki, T. Kamya, H. Hosono, *J. Ceram. Soc. Jpn.* **2012**, 120, 447.

[44] R. Waser, M. Aono, *Nat. Mater.* **2007**, 6, 833.

[45] J. J. Yang, D. B. Strukov, D. R. Stewart, *Nat. Nanotechnol.* **2013**, 8, 13.

[46] C. Schindler, S. C. P. Thermadam, R. Waser, M. N. Kozicki, *IEEE Trans. Electron De vices* **2007**, 54, 2762.

[47] D. S. Jeong, H. Schroeder, R. Waser, *Electrochem. Solid-State Lett.* **2007**, 10, G51.

[48] C. Rohde, B. J. Choi, D. S. Jeong, S. Choi, J.-S. Zhao, C. S. Hwang, *Appl. Phys. Lett.* **2 005**, 86, 262907.

[49] S.-J. Choi, G.-S. Park, K.-H. Kim, S. Cho, W.-Y. Yang, X.-S. Li, J.-H. Moon, K.-J. Lee,

K. Kim, *Adv. Mater.* **2011**, 23, 3272.

[50] F. Zhu, C. H. A. Huan, K. Zhang, A. T. S. Wee, *Thin Solid Films* **2000**, 359, 244.

[51] M. Passlack, E. F. Schubert, W. S. Hobson, M. Hong, N. Moriya, S. N. G. Chu, K. Konstadinidls, J. P. Mannaerts, M. L. Schnoes, G. J. Zydzik, *J. Appl Phys.* **1995**, 77, 686.

[52] C. D. Wagner, A. V. Naumkin, A. Kraut-Vass, J. W. Allison, C. J. Powell, J. R. Jr. Rumble, NIST Standard Reference Database 20, Version 3.4 (web version), http://srdata.nist.gov/xps/, accessed: 4, 2015.

[53] N. Zhou, D. B. Buchholz, G. Zhu, X. Yu, H. Lin, A. Facchetti, T. J. Marks, R. P. H. Chang, *Adv. Mater.* **2013**, 26, 1098.

[54] K. W. Lee, K. M. Kim, K. Y. Heo, S. K. Park, S. K. Lee, H. J. Kim, *Curr. Appl. Phys.* **2011**, 11, 280.

[55] X. Yu, J. Smith, N. Zhou, L. Zeng, P. Guo, Y. Xia, A. Alvarez, S. Aghion, H. Lin, J. Yu, R. P. H. Chang, M. J. Bedzyk, R. Ferragut, T. J. Marks, A. Facchetti, *Proc. Natl. Acad. Sci. USA* **2015**, 112, 3217.

[56] A. Hartmann, M. K. Puchert, R. N. Lamb, *Surface and Interface Anal.* **1996**, 24, 671.

[57] T. Böske, K. Maiti, O. Knauff, K. Ruck, M. S. Golden, G. Krabbes, J. Fink, T. Osafune, N. Motoyama, H. Eisaki, S. Uchida, *Phys. Rev. B* **1998**, 57, 138.

[58] J. P. Espinós, J. Morales, A. Barranco, A. Caballero, J. P. Holgado, A. R. González-Elipe. *J. Phys. Chem. B* **2002**, 106, 6921.

[59] Y. Yao, G. Xie, N. Song, X. H. Yu, R. X. Li, *Advanced Materials Research* **2012**, 399, 2241.

[60] F. Y. Xie, L. Gong, X. Liu, Y. T. Tao, W. H. Zhang, S. H. Chen, H. Meng, J. Chen, *J. Electron Spectrosc. Relat. Phenom.* **2012**, 185, 112.

[61] S.-H. Kim, J.-K. Kim, N. Kwak, H. Sohn, J. Kim, S.-H. Jung, M.-R. Hong, S. H. Lee, J. Collins, *Electrochem. Solid-State Lett.* **2006**, 9, C54.

[62] P. Gao, F. Li, F. Xiao, N. Zhao, N. Sun, W. Wei, L. Zhong, Y. Sun, *Catal. Sci. Technol.*

2012, 2 1447.

[63] I. Barin, O. Knacke, O. Kubaschewski, *Thermochemical Properties of Inorganic Subst ances*, Springer, Berlin, Germany, **1973**.

[64] W. D. Callister, *Materials Science and engineering: an introduction*, John Willey & Sons, Inc., New York, USA, **2003**.

[65] N. Kimizuka, T. Mohri, *J. Solid State Chem.* **1985**, 60, 382.

[66] K. Nomura, T. Kamiya, H. Ohta, T. Uruga, M. Hirano, H. Hosono, *Phys. Rev. B* **2007**, 75, 035212.

[67] J. C. Slater, *J. Chem. Phys.* **1964**, 41, 3199.

[68] R. D. Shannon, *Acta Cryst.* **1976**, A32, 751.